

JGR Atmospheres

RESEARCH ARTICLE

10.1029/2019JD031957

Key Points:

- Formaldehyde and hydrogen peroxide scavenging efficiencies are consistent with literature, while methyl hydrogen peroxide is generally smaller
- Highly soluble hydrogen peroxide is mostly depleted between cloud base and the freezing level, that is, the warm region of the storm
- Retention of dissolved trace gases in frozen precipitation seems to be more important for moderately soluble trace gases

Supporting Information:

- Supporting Information S1

Correspondence to:

G. C. Cuchiara,
 gustavo.cuchiara@colorado.edu

Citation:







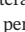








Cuchiara, G. C., Fried, A., Barth, M. C., Bela, M., Homeyer, C. R., Gaubert, B., et al. (2020). Vertical transport, entrainment, and scavenging processes affecting trace gases in a modeled and observed SEAC⁴RS case study. *Journal of Geophysical Research: Atmospheres*, 125, e2019JD031957. <https://doi.org/10.1029/2019JD031957>

Received 4 NOV 2019

Accepted 25 APR 2020

All rights reserved. Accepted article online 29 APR 2020

Vertical Transport, Entrainment, and Scavenging Processes Affecting Trace Gases in a Modeled and Observed SEAC⁴RS Case Study

G. C. Cuchiara^{1,2} , A. Fried¹ , M. C. Barth² , M. Bela^{3,4} , C. R. Homeyer⁵ , B. Gaubert² , J. Walega¹ , P. Weibring¹ , D. Richter¹ , P. Wennberg^{6,7} , J. Crouse⁶ , M. Kim⁶ , G. Diskin⁸ , T. F. Hanisco⁹ , G. M. Wolfe^{9,10} , A. Beyersdorf^{11,12} , J. Peischl³ , I. B. Pollack^{3,13} , J. M. St. Clair^{6,14,15} , S. Woods¹⁶ , S. Tanelli¹⁷ , T. V. Bui¹⁸ , J. Dean-Day¹⁸ , L. G. Huey¹⁹ , and N. Heath²⁰

¹Institute of Arctic and Alpine Research, University of Colorado, Boulder, CO, USA, ²Atmospheric Chemistry Observations and Modeling Laboratory, National Center for Atmospheric Research, Boulder, CO, USA, ³Cooperative Institute for Research in Environmental Sciences, University of Colorado Boulder, Boulder, CO, USA, ⁴Chemical Sciences Laboratory, Earth System Research Laboratory, NOAA, Boulder, CO, USA, ⁵School of Meteorology, University of Oklahoma, Oklahoma, OK, USA, ⁶Division of Geological and Planetary Sciences, California Institute of Technology, Pasadena, CA, USA, ⁷Division of Engineering and Applied Sciences, California Institute of Technology, Pasadena, CA, USA, ⁸Atmospheric Composition, NASA Langley Research Center, Hampton, VA, USA, ⁹Atmospheric Chemistry and Dynamics Laboratory, NASA Goddard Space Flight Center, Greenbelt, MD, USA, ¹⁰Joint Center for Earth Systems Technology, University of Maryland, Baltimore County, Baltimore, MD, USA, ¹¹Chemistry and Dynamics Branch, National Aeronautics and Space Administration, Langley Research Center, Hampton, VA, USA, ¹²Chemistry Department, California State University, San Bernardino, CA, USA, ¹³Now at: Department of Atmospheric Science, Colorado State University, Fort Collins, CO, USA, ¹⁴Now at: Atmospheric Chemistry and Dynamics Laboratory, National Aeronautics and Space Administration, Goddard Space Flight Center, Greenbelt, MD, USA, ¹⁵Now at: Joint Center for Earth Systems Technology, University of Maryland Baltimore County, Baltimore, MD, USA, ¹⁶Stratton Park Engineering Company, Inc., Boulder, CO, USA, ¹⁷Jet Propulsion Laboratory, California Institute of Technology, Pasadena, CA, USA, ¹⁸Bay Area Environmental Research Institute, National Aeronautics and Space Administration, Ames Research Center, Moffett Field, CA, USA, ¹⁹School of Earth and Atmospheric Sciences, Georgia Institute of Technology, Atlanta, GA, USA, ²⁰Department of Earth, Ocean and Atmospheric Science, Florida State University, Tallahassee, FL, USA

Abstract The convectively driven transport of soluble trace gases from the lower to the upper troposphere can occur on timescales of less than an hour, and recent studies suggest that microphysical scavenging is the dominant removal process of tropospheric ozone precursors. We examine the processes responsible for vertical transport, entrainment, and scavenging of soluble ozone precursors (formaldehyde and peroxides) for midlatitude convective storms sampled on 2 September 2013 during the Studies of Emissions, Atmospheric Composition, Clouds and Climate Coupling by Regional Surveys (SEAC⁴RS) study. Cloud-resolving simulations using the Weather Research and Forecasting with Chemistry model combined with aircraft measurements were performed to understand the effect of entrainment, scavenging efficiency (SE), and ice physics processes on these trace gases. Analysis of the observations revealed that the SEs of formaldehyde (43–53%) and hydrogen peroxide (~80–90%) were consistent between SEAC⁴RS storms and the severe convection observed during the Deep Convective Clouds and Chemistry Experiment (DC3) campaign. However, methyl hydrogen peroxide SE was generally smaller in the SEAC⁴RS storms (4%–27%) compared to DC3 convection. Predicted ice retention factors exhibit different values for some species compared to DC3, and we attribute these differences to variations in net precipitation production. The analyses show that much larger production of precipitation between condensation and freezing levels for DC3 severe convection compared to smaller SEAC⁴RS storms is largely responsible for the lower amount of soluble gases transported to colder temperatures, reducing the amount of soluble gases which eventually interact with cloud ice particles.

1. Introduction

The formation and development of convective clouds are the most important mechanisms for vertical transport and redistribution of tropospheric pollutant gases or trace species (Dickerson et al., 1987). The

convectively driven vertical transport of these trace gases from the planetary boundary layer (PBL) to the upper troposphere (UT) can occur on timescales of less than an hour (Chatfield & Crutzen, 1984) leading to a rapid and direct change in the abundance of trace gases deposited in the UT. In many cases, these convectively transported trace gases can have an impact on ozone (O_3) in the UT through subsequent chemical reactions involving HO_x (where $HO_x = OH + HO_2$) radicals (Pickering et al., 1992; Cooper et al., 2009). For example, Pickering et al. (1992) estimated that convective transport of urban plumes could account for 30% more O_3 in the entire tropospheric column in the first 24 hr after convection initiation. The chemistry in the convective outflow regions can impact regional air quality far removed from their local emission sources via enhanced horizontal winds that are prevalent in the UT followed by subsequent downward transport (Betts et al., 2002; Dickerson et al., 1987; Gerken et al., 2016).

The first UT HO_x measurements were collected in 1996 during the STRAT campaign over the tropical Pacific Ocean (Jaeglé et al., 1997). Results from this campaign showed that convective transport of HO_x precursors can be a factor of two or more greater than those expected in the literature (Jaeglé et al., 1997). The convective process can also remove large fractions of soluble HO_x radical precursors like formaldehyde (CH_2O), hydrogen peroxide (H_2O_2), and methyl hydrogen peroxide (CH_3OOH) through scavenging. Furthermore, many authors (Finlayson-Pitts & Pitts, 1986; Jaeglé et al., 2000; Jaeglé et al., 1997; Falouana et al., 2000) suggested that in the UT, where the water vapor is limited, H_2O_2 , CH_3OOH , and CH_2O become important HO_x reservoir species.

Previous studies using slightly different methods for various locations have also examined the convective redistribution of HO_x precursors. Analysis of oceanic convection sampled during Pacific Exploratory Missions in the Tropics (PEM-Tropics) over the South Pacific found the scavenging efficiency (SE) of H_2O_2 to be 55–70% and CH_3OOH to be negligible (Cohan et al., 1999). Using a one-dimensional convective plume model, Mari et al. (2000) estimated SEs of 23% for CH_2O , 66% for H_2O_2 , and 5% for CH_3OOH in the convective cores of storms. Borbon et al. (2012) report a rather large range for CH_2O SEs from 4% to 39% for four severe storms during the African Monsoon Multidisciplinary Analysis (AMMA) study. Based on aircraft measurements of 20 flights extending from California to the mid North Atlantic, Snow et al. (2007) found enhanced CH_2O , CH_3OOH , and depletion of H_2O_2 and HNO_3 on convective outflow compared to background UT. The studies by Cohan et al. (1999), and Borbon et al. (2012) were based on observations in the outflow region and in clear air profiles and employed a very simple entrainment model. Using a high-resolution 3-D cloud chemistry model to represent a severe thunderstorm, Barth, Kim, Skamarock, et al. (2007) compared the flux to the ground of the dissolved trace gas in precipitation to the flux of the trace gas into cloud base and found SEs of 45–57% for CH_2O , 55–60% for H_2O_2 , and ~7% for CH_3OOH , even though simulated gas-phase CH_2O was predicted to be <50 parts-per-trillion by volume (pptv) in the convective outflow region, which would imply a much higher SE. However, much of the remaining CH_2O was tied up in the modeled cloud particles that had not rained out. A comparison of deep convective transport of several trace gases among several cloud-resolving three-dimensional models revealed good agreement of convective outflow mixing ratios for insoluble trace gases like CO, but significant disagreement of convective outflow mixing ratios for CH_2O and H_2O_2 (Barth, Kim, Wang, et al., 2007).

A more comprehensive analysis was carried out during the 2012 Deep Convective Clouds and Chemistry (DC3, Barth et al., 2015) campaign, which focused on a better understanding of how deep convective clouds in the continental midlatitudes impact UT chemical composition through convective transport, lightning NO_x production, wet removal, surface sources, dynamics, and UT chemistry. DC3 had the advantage over previous studies in that two fully instrumented aircraft flew in close coordination to sample convective inflow and outflow regions in near-simultaneous fashion. During DC3 campaign, the sampled storms formed in distinct dynamic and chemical environments, thus allowing for SE determinations for CH_2O , H_2O_2 , and CH_3OOH over a range of conditions. Fried et al. (2016) determined CH_2O SEs of 41–58%, and Barth et al. (2016) determined H_2O_2 and CH_3OOH SEs of 79–97% and 12–84%, respectively, during DC3. Fried et al. (2016) and Barth et al. (2016) further employed the ratio of the organic tracers *i/n*-butane and *i/n*-pentane measured in the inflow and outflow as a means to ensure that these air masses were coherently related (i.e., when these ratios were similar, the inflow and outflow regions did not have vastly different origins). As shown by Fried et al. (2016), the coherence between inflow and outflow is important for accurate SE determinations and may explain the much larger

range of SEs determined for CH₂O from past studies. Analysis of cloud-resolving simulations (horizontal grid spacing ≤ 3 km) of one DC3 storm (Bela et al., 2016) found similar SEs as those reported by Fried et al. (2016) and Barth et al. (2016), including the higher-than-expected SE for CH₃OOH. More recently, Bela et al. (2018) analyzed cloud-resolving simulations of three DC3 storms to determine the processes responsible for producing the simulated SEs. Bela et al. (2018) suggest that the CH₃OOH outflow mixing ratios were decreased mainly by entrainment of cleaner background air as well as by liquid and mixed-phase scavenging. They also found that CH₂O and H₂O₂ mixing ratios were more affected by liquid phase scavenging than by entrainment or aqueous chemistry.

While the DC3 study provided a solid foundation to improve our understanding of convective transport of soluble O₃ precursors, the storms studied were primarily severe convection. Additional studies over a broader variety of storms with larger differences in vertical velocities and liquid water contents are needed to advance our understanding even further. One of the objectives of the Studies of Emissions, Atmospheric Composition, Clouds and Climate Coupling by Regional Surveys (SEAC⁴RS) field campaign was to sample trace gases and aerosols in deep convective outflow to examine the subsequent impact on UT composition (Toon et al., 2016). During August and September 2013, the NASA DC-8 aircraft sampled the inflow and outflow of several deep convective storms over the south and southeast U.S. and over the Gulf of Mexico. The sampled storms were much weaker than those reported previously in the literature, allowing us to address the first objective of this paper by extending the current knowledge of SEs to airmass and multicell convective systems.

A second objective of this study is to address the complex role of ice in the scavenging processes of CH₂O and peroxides during convective transport. As air masses ascend in convection, ice, and subsequently snow and graupel, form at higher altitudes. The dissolution of gases like CH₂O and H₂O₂, for example, could be significantly altered as droplets freeze. A parameter called the ice retention factor (rf = fraction of trace gas retained in an ice particle when cloud drops freeze), which ranges in value from 0 to 1, is used in modeling studies to adjust the trace gas partitioning between gas and condensed phases in the presence of ice (Leriche et al., 2013 and references therein). Many previous studies investigated phase partitioning during liquid-to-solid freezing and riming to better understand and represent these effects (Jost et al., 2017; Snider & Huang, 1998; Stuart & Jacobson, 2004, 2006; Voisin et al., 2000; von Blohn et al., 2011). At present, there is a large range of reported rf values, which can create uncertainties in model predictions of convective transport of HO_x precursors and subsequent O₃ chemistry. For example, Leriche et al. (2013) showed, with cloud-resolving simulations of gaseous- and aqueous-phase chemistry and cloud physics effects on trace gases, that CH₂O mixing ratios in the UT were sensitive to the ice retention factor value. Combining a semiempirical model and wind tunnel measurements, Jost et al. (2017) found that rf for CH₂O can be as high as 0.97. In contrast, Bela et al. (2018) and Fried et al. (2016) showed that WRF-Chem model simulations of CH₂O scavenging can only be reconciled with aircraft observations during the severe 29 May 2012, DC3 storm case using $rf < 0.25$. The ice retention factors have also been shown to be important for parameterized convective transport and scavenging. After adding ice retention factors for various species and adjusting the conversion rate of cloud water to rainwater at temperatures below freezing in the Grell-Freitas convective parameterization, Li et al. (2019) improved the representation of cloud-parameterized wet scavenging and found $rf = 0$ gave the best agreement with observed CH₂O SEs for the 29 May DC3 storm. The discrepancies among these different studies highlight the importance of further examining rf for CH₂O as well as the other trace gases discussed above.

A third objective of this study is to reexamine the role that enhanced NO_x may have on deduced SEs for CH₂O and the peroxides. During some of the DC3 intercepts, the aircraft sampled air with enhanced NO_x from lightning, but these outflow intercepts did not show any effect on the determined SEs for CH₂O and H₂O₂. Nevertheless, enhanced NO_x from lightning (LNO_x) could yield erroneous calculated SEs for CH₂O, CH₃OOH, and H₂O₂ if not properly accounted for. This effect, which will be further discussed below, will not only depend upon the enhanced NO_x levels but also the VOC levels convectively lofted to the UT and the NO_x interaction times. The impact of LNO_x on trace gas transport can be quite important, as many convective studies would be expected to encounter enhanced NO_x from lightning, as is the case for some of the higher altitude measurements sampled in this study. These measurements thus provided us with an additional opportunity to examine the effects of lightning NO_x on CH₂O, CH₃OOH, and H₂O₂ SEs.

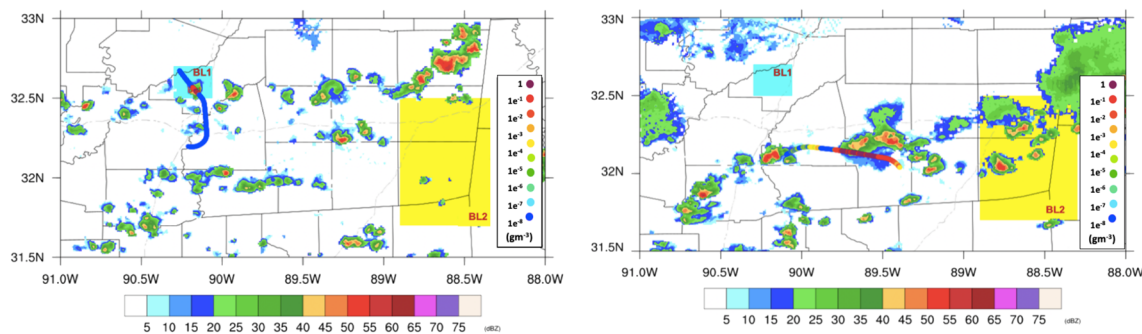


Figure 1. DC-8 flight track at (a) ca. 8 km in storm Core 2/Intercept 4 at 18:16 UTC over the BL1 inflow region (blue square), and (b) ca. 12 km in storm Core 7/Intercept 14 at 19:53 UTC near the BL2 region (yellow square). The flight track is colored by IWC (g m^{-3}) overlaid on NEXRAD composite radar imagery (dBZ) at (a) 18:15 UTC and (b) 20:05 UTC.

In addition to CH_2O , H_2O_2 , and CH_3OOH SE calculations, we also present here the SEs for hydroxymethyl hydrogen peroxide ($\text{HOCH}_2\text{O}_2\text{H}$, HMHP) and SO_2 . HMHP contributes to gas-phase atmospheric chemistry through its OH oxidation to form formaldehyde and formic acid (Allen et al., 2018), yet is highly soluble and subject to wet scavenging and aqueous-phase chemistry in clouds (O'Sullivan et al., 1996). Thus, it is important to establish HMHP SEs from observations.

This work combines both observational techniques and modeling approaches in studying convection for various storm intercepts on 2 September 2013 over Mississippi during the SEAC⁴RS campaign. We present an analysis of prefrontal continental convection for both an isolated airmass storm as well as a more mature multicellular storm. As will be described in a later section, SEs for various trace gases are determined by comparing the mixing ratios in the outflow regions to the inflow regions after accounting for dilution by entrainment. The SEs derived from observations are then compared to SEs determined from cloud-scale model simulations that use different rf values to estimate the most appropriate rf for the studied storms. We conclude by highlighting the importance of rf , LNO_x, and cloud physics for analyzing effects of thunderstorms on ozone precursors.

2. Case Study Description and Data

2.1. Overview of SEAC⁴RS Storm Cases

This work analyzes storms on 2 September 2013, when a surface low pressure system north of the Great Lakes with an associated front extending through the southwest portions of Texas occurred at 18:00 UTC (Figure S1 in the supporting information). During this day, the gradients associated with the frontal system led to the development of convection and outflow boundaries associated with airmass storms (Heath et al., 2017). This study analyzes NASA DC-8 aircraft observations penetrating the pre-frontal convection around Jackson, Mississippi (Figure S1).

The aircraft collected measurements in the storm inflow region at approximately 16:53 UTC starting at low altitudes (~ 0.79 km) to characterize the composition of the PBL (BL1 in Figure 1) just prior to the convective initiation ($\sim 17:50$ UTC). The aircraft then ascended to ~ 8 km altitude above mean sea level and intercepted newly-formed convective cells ($\sim 17:54$ to 18:23 UTC) in a developed west-to-northeast oriented line of ordinary airmass storms (Intercepts 2–5 in Table S1 give the start and end times for all intercepts). Next, the DC-8 aircraft climbed to ~ 12 km altitude where it sampled a second line of more mature convective storms mainly in the anvils and decaying stratiform precipitation region from 19:31 to 19:54 (Intercepts 11 and 14 in Table S1). Afterward, the aircraft descended to the PBL again and sampled air being ingested in later convective storms (BL2 in Figure 1) at low altitudes of about 0.41 km. The entire DC-8 aircraft flight resulted in 22 individual convective outflow intercepts (Table S1) of eight distinctive storms, classified here by their duration, intensity, vertical development, proximity to the inflow sampling region, and the number of convective cores in the thunderstorm cloud. The eight intercepted convective clouds are shown in Figure S2 and tabulated in Table S1 under the classification “Cloud Cores.” The relatively close proximity to the National Weather Service WSR-88D ground-based radar from Jackson, MS (KDGX) provided a

strong data set when the ~5 min interval NEXRAD level-II reflectivity (Crum & Albrecht, 1993) were combined with the aircraft measurements. Additional details will be given in section 2.2.

This study is focused on Outflow Intercepts 2–5 (~8 km), carried out on what we designate as storm Cloud Core 2, an evolving isolated airmass storm (~55 min duration) in the first line of convective cells, and Outflow Intercepts 11 and 14 (~12 km) carried out on what we designate as storm Cloud Core 7. The latter is a more mature multicellular storm (~3 hr duration) in the second line of convection. Core 2 and Core 7 were selected due to their distinct cloud depth (~8 and ~12 km height, respectively), horizontal proximity of the storm core with the PBL inflow regions, and the characteristic of the convective core (single and multicellular core, respectively). The winds during Intercepts 2–5 from Core 2, furthermore, were uniform in both direction and magnitude, allowing multiple intercepts of the same isolated storm core. The radar imagery relative to the DC-8 flight track was used to identify the evolving storm cores (Figure 1). Figure 1a shows the DC-8 flight track for Outflow Intercept 4 of storm Core 2 measured within the ~55-min storm lifetime. The radar images at ~8 km (not shown) indicate core intercepts occurring in a range of reflectivities between 10 and 30 dBZ and a range of peak ice water contents (IWC) from the High-Volume Precipitation Spectrometer version 3 (HVPS-3) of 0.6 to 1.5 g m⁻³ for Intercepts 2–5, and peak vertical velocities (w) of 15 m s⁻¹ based on the MMS measurements (the Airborne Second Generation Precipitation Radar—2 (APR-2) data recorded peak w of 9 m s⁻¹ for Intercept 2 and 2–4 m s⁻¹ for Outflow Intercepts 3–5. Figure 1b shows the flight track for Outflow Intercept 14 of storm Core 7 at ~12 km. This intercept had radar reflectivities at 12 km ranging from 10–25 dBZ, a peak IWC of 0.6 g m⁻³, and w of 5–8 m s⁻¹ (the aircraft did not directly fly through the Core 7 updraft). We note that the aircraft intercepted the outflow just downwind (to the southwest) of the updraft in the case of Core 7.

It is important to note the major differences in the storm intercepts of this study and those encountered during DC3. During the 29 May 2012 severe DC3 convective storm, the maximum vertical velocities, derived from dual-Doppler radar analysis, ranged between 20 and 60 m s⁻¹ (DiGangi et al., 2016), compared to ≤ 15 m s⁻¹ (determined from aircraft measurements at the top of the storm core) in this study. DC3 convective outflow sampling was not directly at the top of updraft cores due to safety reasons, but instead were in the much larger anvil outflow regions. DC3 outflow intercepts were often as long as 10-min in duration and 10–60 min downwind of the core. By contrast, the SEAC⁴RS intercepts of this study sampled directly through the updraft cores or <5 min downwind of the core multiple times at different altitudes. As a consequence, the present study does not employ the core extrapolation method discussed by Fried et al. (2016) for DC3, thereby reducing one source of uncertainty. However, the SEAC⁴RS isolated airmass intercept times ranged from 5–10 s, which corresponds to ~1,050–2,400 m in distance at ~210–240 m s⁻¹ airspeed. For this reason, in contrast to DC3, we could not use the Whole Air Sampler (WAS) measurements, which generally had sampling times significantly longer than the cloud intercepts. Furthermore, such fast SEAC⁴RS core intercepts did not allow us to rely on fast PTRMS measurements of benzene and toluene, which due to the scanning nature of those measurements, were not acquired simultaneously and often missed the storm core peaks. Hence, all SEAC⁴RS core intercepts relied on fast measurements of CO and carbon dioxide (CO₂) as airmass tracers and careful analysis of NEXRAD radar images as well as WRF simulations to ensure coherence between inflow and outflow regions.

2.2. Data

The meteorological and chemical measurements used in this work include instruments aboard the DC-8 aircraft, ground-based radar, and radiosonde measurements. The aircraft meteorological measurements included air temperature, winds, ice and liquid water content, radar reflectivity, vertical velocity, and hydrometeor classification. The Meteorological Measurement System (MMS; Chan et al., 1998) provided air temperature and flight-level three-dimensional winds with 0.1 m s⁻¹ precision from vertical velocity measurements. The Stratton Park Engineering Company Incorporated (SPEC) HVPS-3 (Lawson et al., 1998) measured IWC based on particle sizes ranging from 150 to 19,200 microns. The APR-2 images aided the identification of cloud characteristics. The APR-2 (Sadowy et al., 2003), a dual-frequency (13 and 35 GHz) dual-polarization Doppler radar system, used a downward antenna to perform cross-track scans of the cloud intercepts allowing the analysis of the microphysical structure of the cloud. A collection of APR-2 curtain plots of radar reflectivity, vertical velocity, and hydrometeor classification for selected storm clouds are provided in Figure S3. In general, the APR-2 results show a similar range of Ku-band reflectivity and

Doppler velocity for intercepts of both air mass (the first and second column Figure S3a) and multicellular storms (first and second column Figure S3b). The hydrometeor classification (Figure S3 third column) plots show large regions of dry ice with some smaller regions of dry and wet graupel relatively close to the altitude where the DC-8 intercepted the convective storms. Data from individual NEXRAD radars are merged into hourly, high-resolution, three-dimensional, gridded, synoptic analyses using weighting in space and time. Additional details can be found in the Gridded NEXRAD WSR-88D Radar (GridRad) algorithm description document (Homeyer & Bowman, 2017). The observed vertical profiles of temperature, dewpoint temperature, and winds were derived from the NOAA National Weather Service radiosonde from Jackson Thompson Field (JAN—72235—32.32°N, 90.08°W) released at 12:00 UTC.

CH₂O was measured on the DC-8 aircraft by two instruments, the University of Colorado Compact Atmospheric Multispecies Spectrometer (CAMS; Richter et al., 2015) and the NASA Goddard Space Flight Center In situ Airborne Formaldehyde (ISAF) system (Cazorla et al., 2015). CAMS is a mid-IR laser-based absorption spectrometer, which provided CH₂O data with 1–2 s temporal resolution with an estimated accuracy and limits of detection (LODs at 1 σ) of around 4% and ~40 to 60 pptv, respectively. The ISAF instrument detects CH₂O using UV-laser-induced fluorescence (LIF) at 1 Hz with a LOD of ~36 pptv (S/N = 2 and 1 s integration) and an estimated accuracy of 10% (Cazorla et al., 2015). The results for the two instruments were compared by Morgan Silverman and Gao Chen at NASA Langley (see Figure S4) over the entire SEAC⁴RS study employing a 10-s merge for data above the respective instrument detection limits and where each instrument had data coverage for at least 70% of each 10-s bin. An orthogonal distance regression (ODR) of the ISAF results (Y-axis, labeled LIF) versus the CAMS data (X-axis), with one outlier removed, produced the following regression: [ISAF] = (87 \pm 6) pptv + (1.085 \pm 0.002) \times [CAMS], $R^2 = 0.91$. We combined these two data sets arbitrarily: (1) applying a modification to the ISAF data ([ISAF]–87 pptv/1.085) to derive CH₂O mixing ratios on the CAMS scale, followed by (2) computation of the average of the two measurements (CAMS and adjusted ISAF data). The peak mixing ratios from the two instruments in the various outflows typically differed by 3 s (CAMS lagged ISAF), and the adjustments and average values were determined by first shifting the CAMS data by negative 3 s. We note that employing a different combination of the two CH₂O data sets only negligibly changes the final CH₂O SE results. For example, combining the two data sets using a straight average from the two instruments without applying the above regression, with CAMS first shifted by negative 3 s and linearly interpolating CAMS data to account for missing points during frequent zeroing, only changed the resulting CH₂O SEs by a maximum of 0.3%–0.5% for the various periods investigated.

The peroxides were measured on the DC-8 with the time-of-flight (ToF-CIMS) mass filter and tandem quadrupole mass filter (T-CIMS) chemical ionization mass spectrometers (CIMS) utilizing reaction with CF₃O[–] (Amelynck et al., 2000; Crouse et al., 2006; Huey et al., 1996; St. Clair et al., 2010). These data were obtained at high temporal resolution (1 Hz or faster) with uncertainties for H₂O₂ and HOCH₂O₂H of 50 pptv + 0.3 \times [H₂O₂] and 20 pptv + 0.5 \times [HOCH₂O₂H], respectively. Ambient CH₃OOH data are provided as the fraction of an isotopically labeled standard addition. While there is confidence in the computed fraction (and thus, the variability of ambient CH₃OOH), there are additional uncertainties of the standard addition output making it difficult to calculate absolute ambient mixing ratios of CH₃OOH. Nevertheless, the CH₃OOH/internal standard ratios could still be used to determine CH₃OOH SEs in a manner similar to the mixing ratios for the other species. Potential bias in CH₃OOH observations within the boundary layer during the DC3 and SEAC⁴RS experiments could lead to overestimation of the calculated SEs (see Text S1 for more information).

SO₂ was measured by a custom-built chemical ionization mass spectrometer (Kim et al., 2007). The instrument was calibrated nearly continuously by standard addition of an isotopically labeled standard. Data were collected at 1 Hz with estimated uncertainties of 15%.

CO₂ and CO were selected to represent tracer transport. CO₂ was measured with the Atmospheric Vertical Observation of CO₂ in the Earth's Troposphere (AVOCET) instrument, a nondispersive infrared spectrometer (Vay et al., 2011). CO was measured by the Differential Absorption CO Measurement instrument (DACOM), which is a 4.5- μ m tunable diode laser (Sachse et al., 1987). In addition, measurements of NO, NO₂, and O₃ were collected with the NOAA nitrogen oxides and ozone (NO_yO₃) 4-channel chemiluminescence (CL) instrument (Pollack et al., 2010; Ryerson et al., 2000).

3. Model Description and Evaluation

3.1. Model Configuration

The Weather Research and Forecast with Chemistry (WRF-Chem) model (Fast et al., 2006; Grell et al., 2005) version 3.9.1 was used in this study. WRF coupled with artificial tracers (WRF-tracer) and WRF coupled with chemistry (WRF-Chem) simulations were performed for the 2 September storm to (1) predict transport and entrainment of soluble trace gases in convection; (2) to analyze processes, especially ice retention factors, which affect scavenging; and (3) utilize parts of the chemistry packages in the code to model how boundary layer species concentrations change over the day (important when considering BL2) as well as aid in the analysis of the effects of lightning-enhanced NO on the various species concentrations in the outflow. This case presented extra challenges for WRF-Chem model simulations due to the relatively small size of the clouds, the location, and the time of the convective initiation. Much of the model configuration follows that of Heath et al. (2017) with additional testing (Text S2) to best represent the observed convection.

WRF-Chem was run for an 18-hr simulation period and initialized on 2 September at 06 UTC, 2013. The first 6 hr of the simulation were considered spin-up, and the model results of the last 12-hr simulation period were used for further analysis. Three model domains are centered over the DC-8 aircraft intercept sampling region for the 2 September storms (Figure S5 and Fig. 2 of Heath et al., 2017). The domains range in resolution from coarse (Domains 1 and 2, $\Delta x = 12.15$ km and $\Delta x = 4.05$ km, respectively), with parameterized convection (Table S2), to convective-permitting (Domain 1 $\Delta x = 1.35$ km with no parameterized convective scheme). The cumulus scheme was turned off in the inner domain to allow an explicit representation of the convection. All three domains have 74 vertical levels from the surface (~ 100 m) to 100 hPa, vertical resolution of $dz \approx 100$ m in the lowest levels, and $dz \approx 250$ m from above the PBL into the stratosphere.

To initialize trace gas and aerosol mixing ratios as well as provide lateral boundary conditions, 6-hourly results from the Community Atmosphere Model with Chemistry (CAM-Chem) are used (Tilmes et al., 2015). CAM-Chem was run at $1.25^\circ \times 0.9^\circ$ horizontal resolution and 32 vertical layers. The chemistry package of WRF was turned on for all domains using the Model for Ozone and Related chemical Tracers (MOZART) gas-phase chemical mechanism and the Global Ozone Chemistry Aerosol Radiation and Transport (GOCART) scheme for aerosols (Pfister et al., 2011). The Model of Emissions of Gases and Aerosols from Nature (MEGAN v2.04; Guenther et al., 2006) was used to represent the net biogenic emissions, both gases and aerosols. A reduction of 50% in the calculation of biogenic isoprene was applied in order to account for overpredictions recently reported for the southeast U.S. during field campaigns (Carlton & Baker, 2011; Kaiser et al., 2018; Travis et al., 2016; Warneke et al., 2010; Wolfe et al., 2016). Many of those studies suggest that the model-measurement discrepancies and differences among emission inventories approach a factor of two or more. To represent anthropogenic emissions during weekdays and weekend, the simulation uses the National Emission Inventory (NEI—2011), version 2 which correct VOC speciation profiles for oil and gas sources (Bahreini et al., 2018; McDonald et al., 2018). A Sunday emission inventory was used to represent the Monday of 2 September, which was the U.S. Labor Day holiday. The Fire Inventory from NCAR version 1 (FINNV1.6; Wiedinmyer et al., 2011) was implemented to provide daily varying emissions of trace species from biomass burning.

3.2. Model Evaluation of Meteorology

To utilize WRF-Chem for understanding the processes affecting the observationally derived SEs, the simulated microphysical structure of the storms and the vertical profile of the atmosphere need to be evaluated.

3.2.1. Convection Evaluation

A broad overview of the simulated convection is performed by contrasting the radar reflectivity simulated online in the Morrison microphysics scheme (using the Rayleigh approximation at a wavelength of 10 cm) with ground-based radar observations. NEXRAD radar reflectivity images of the storm cores (Figure 2a) show storm formation near the city of Jackson, MS at 18:00 UTC, while the WRF simulation results (Figure 2b) show storm initiation at 18:55 UTC (i.e., 55 min later than the observation). Regardless of the difference in the timing and location of the convection, the scattered convection in the WRF simulation reasonably represents the convective clouds intercepted by the DC-8 aircraft. In particular, the observed and modeled cloud reflectivity magnitudes (45–50 dBZ) are similar.

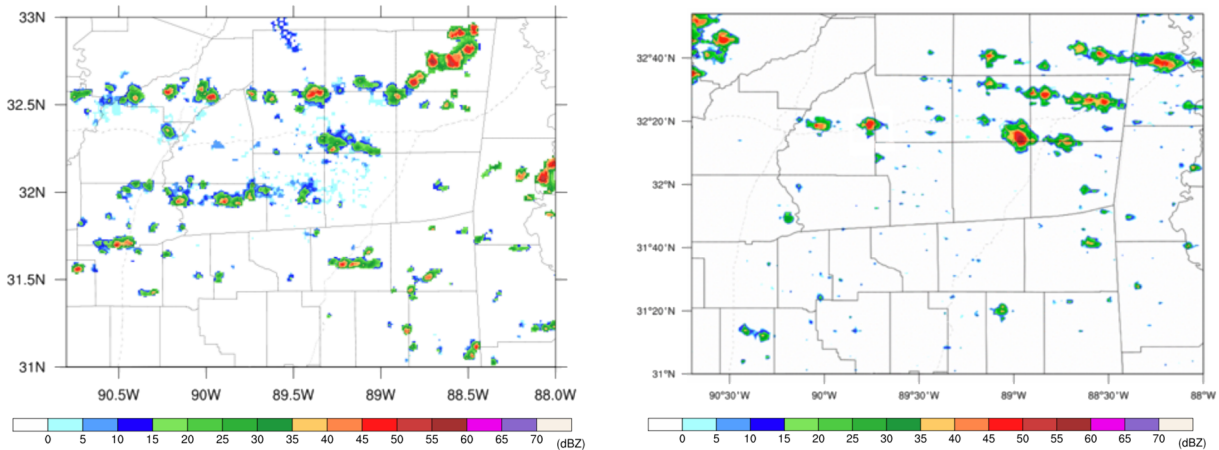


Figure 2. Maximum S-band (10 cm) reflectivity at 1 km a.g.l from (a) retrieved from the Jackson, MS (KDGX) WSR-88D radar at 18:00 UTC and (b) from the WRF model simulation at 18:55 UTC on 2 September 2013.

To further ensure that the simulation faithfully captures the observed thermodynamically vertical structure of the atmosphere and the convection, the Jackson Thompson Field radiosonde and radar reflectivities observation are compared with the WRF-Chem simulated vertical profiles (temperature, dew point, and winds) and reflectivities. The reflectivities were compared using the contoured frequency by altitude diagrams (CFADs) in two different precipitation regimes following Heath et al. (2017). A complete discussion of the results is presented in Text S3, Figures S6–S8, and Table S3. Although WRF displayed some bias in the timing, intensity and location of the convection, the modeled vertical structure of the atmosphere a few hours before the development of the storms was well represented and the vertical structure of the radar reflectivity compared well with observations. The WRF-Chem simulated reflectivity tended to overestimate by 5% the observed NEXRAD reflectivities for the region and study period. This analysis gives confidence that the model is representing a very similar thermodynamic and atmospheric structure, permitting the comparison between model and observations with the simulation of tracers and chemistry.

A few individual simulated clouds were selected to perform a more detailed analysis and to represent the ones measured by the DC-8 aircraft. The simulated clouds were selected within the region and time where the convection validation was performed with the CFAD methodology. In a first analysis, a total of six simulated clouds (called Cores A–F) were selected using the criteria of radar reflectivity between 5–30 dBZ, cloud IWC $QICE > 0.00001 \text{ g kg}^{-1}$, and positive vertical velocities at altitudes where the DC-8 aircraft intercepted the observed convective Cores 2 and 7 (~8 and 12 km, respectively). In a more detailed selection, two storm cloud cores were designated to represent the microphysical characteristics of the observed clouds (section 2.1). Simulated cloud core C was chosen to best represent the airmass storm cloud Core 2, containing 12 grid cells in the outflow region at 8.2 km height, 1.23 g m^{-3} of IWC ($QICE + QSNOW + QGRAUPEL$), and an average of $15 \pm 4 \text{ dBZ}$. The WRF cloud has about twice the IWCs and a 50% higher reflectivity than the observed cloud. The simulated cloud core A was selected to best represent the observed multicellular storm Core 7 with nine grid cells in the outflow region at 10.8 km height containing 0.56 g m^{-3} of IWC, and an average of $8.43 \pm 4.18 \text{ dBZ}$. The grid cells containing these characteristics were identified as the convective core outflow regions of the simulated clouds and were used to perform the entrainment rates, SES, and rf calculations. As we will show, the deduced rf results from the WRF simulations are particularly sensitive to the precise representation of the storm outflow, and this required special effort to carefully identify the optimum cloud core simulations.

3.2.2. Chemistry Evaluation

The performance of the chemistry simulation was evaluated using averaged observed and modeled clear air (CA) profiles (Figure 3) of (a) CH_2O , (b) H_2O_2 , (c) SO_2 , (d) CO , and (e) O_3 for the period between 16:00 and 22:00 UTC along the DC-8 flight track (Figure 6). The CA profiles were obtained from DC-8 sampling periods satisfying the following criteria: (1) flight tracks within the geographic box defined in Figure 4, which

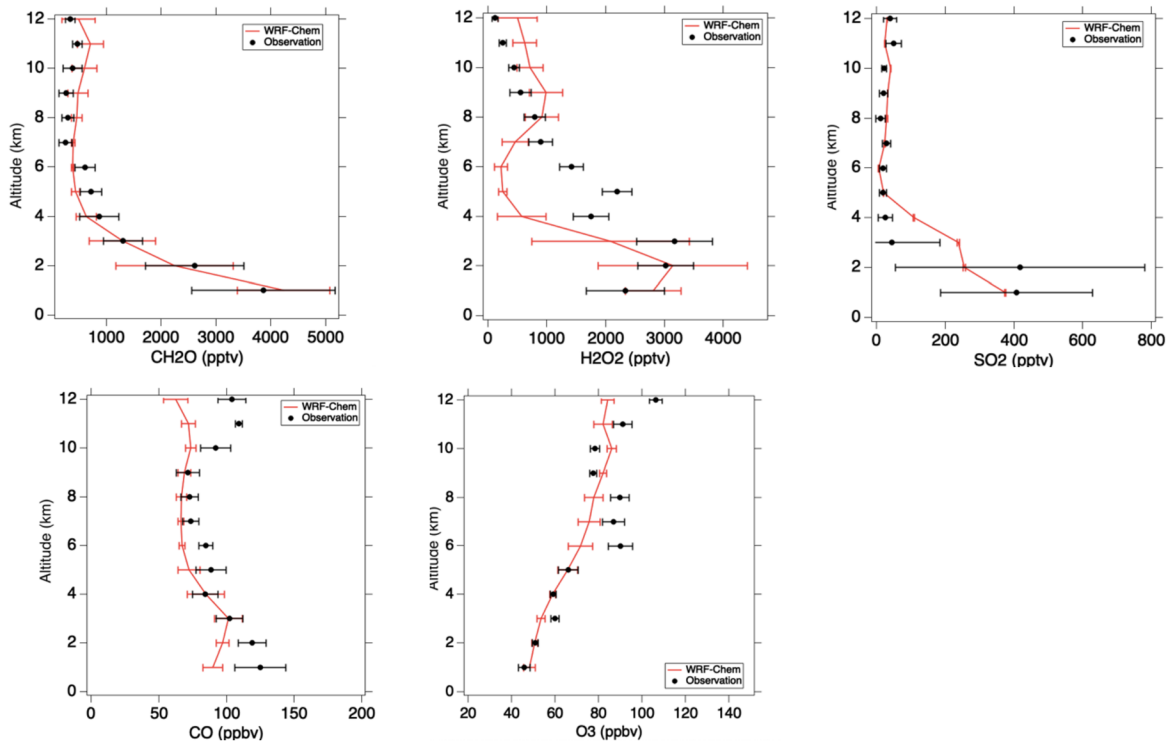


Figure 3. Comparison between clear air vertical profiles of observed (means and standard deviations of 1-km altitude bins) and modeled (a) CH₂O, (b) H₂O₂, (c) SO₂, (d) CO, and (e) O₃ from 16:00 to 22:00 UTC along the DC-8 flight track.

includes all the outflow and BL flight legs over the full altitude range sampled (near surface to 12 km); (2) when the aircraft flight videos and 2-DS cloud probe indicated sampling in cloud-free air (i.e., LWC + IWC < 0.001 g m⁻³); and (3) an upper limit of 1.25 in the O₃/CO ratio to eliminate stratospheric

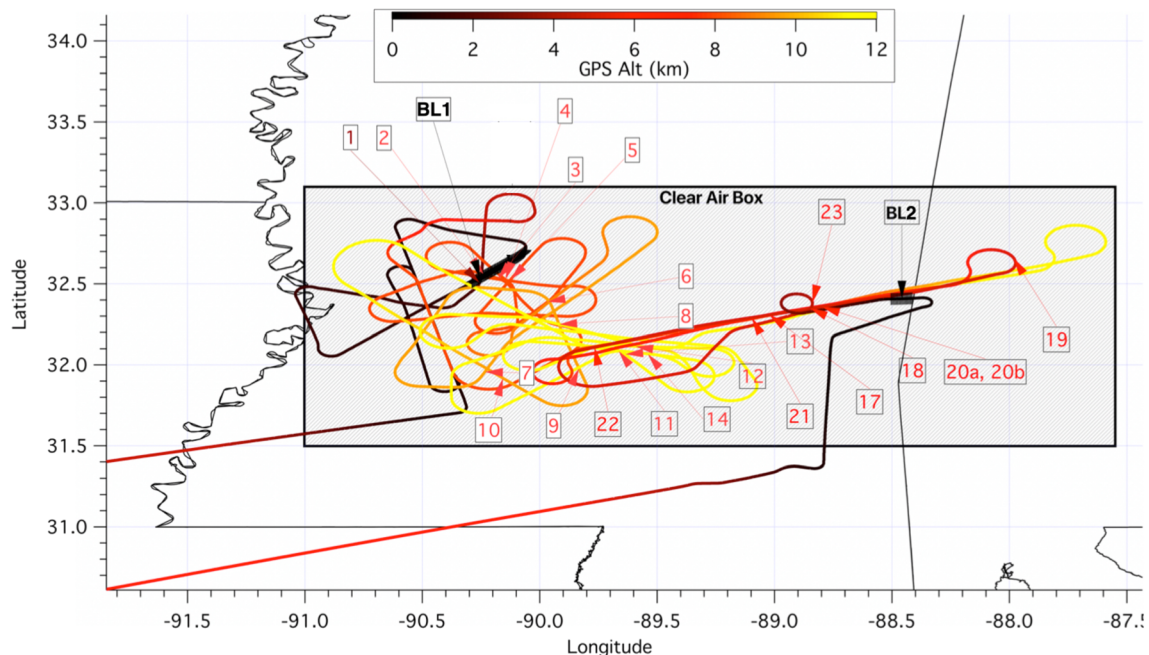


Figure 4. The Clear Air region defined by flights within the latitude range 31.5° N to 33.1° N, and within the longitude range -91.0° W to -87.550° W. The intercept numbers, which are given in Table S1 along with the two BL intercepts (BL1, and BL2).

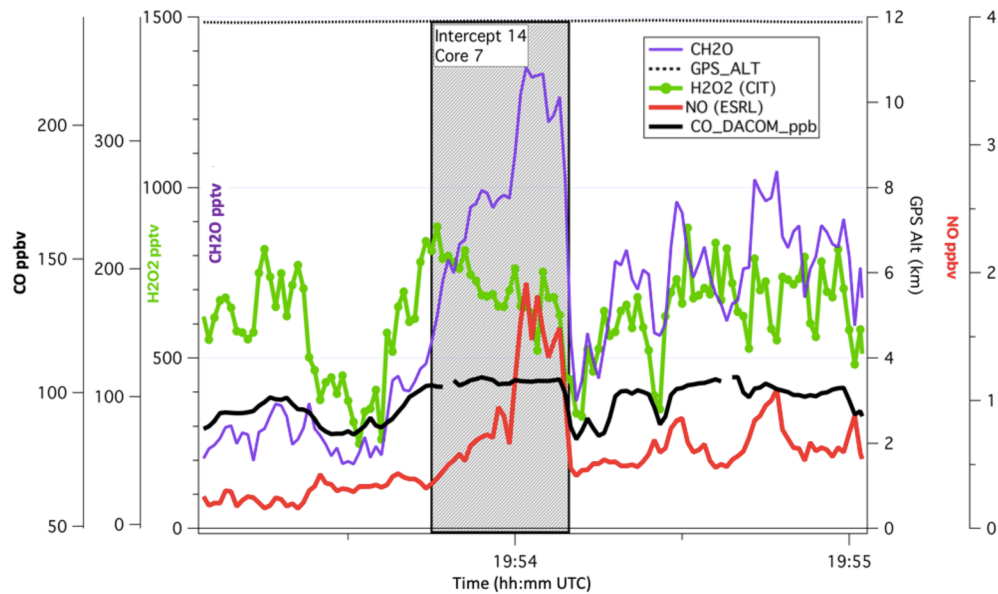


Figure 5. DC-8 measurements for Intercept 14 (storm Core 7) showing enhanced NO (red line) from lightning in the vicinity of enhanced measured CH₂O (purple line) in the convective outflow, and the H₂O₂ depression (green line). The shaded region represents the portion of the outflow where CO is approximately constant (black line) and hence the changes in CH₂O and H₂O₂ are due to chemistry and not changes in dilution.

air, which would add another dilution element in the outflow not captured by our lateral entrainment model. WRF-Chem CA profiles were obtained from grid cells with total condensate (i.e., QCLOUD + QRAIN + QSNOW + QICE + QGRAUPEL) < 0.00001 g kg⁻¹ for the same geographic region shown in Figure 4. In addition to providing measurement-model comparisons, the 1-km altitude binned CA measurements also provided the background concentrations employed in our entrainment calculations, which will be further discussed in section 4.2. Note that no comparison for CH₃OOH is presented due to the lack of mixing ratio values for this species. Table S4 provides the statistical analysis of model results experiments versus observed DC-8 data along the flight track.

The CA vertical profiles have high correlation coefficients (*R*) and small root mean squared errors (RMSE) for CH₂O (*R* = 0.98 and RMSE = 239 pptv), SO₂ (*R* = 0.84 and RMSE = 78 pptv), and O₃ (*R* = 0.88 and RMSE = 10 ppbv). While modeled H₂O₂ profiles match observations fairly well below 4 km and above 7 km altitude, WRF-Chem largely underestimates the observations in the mid-troposphere (*R* = 0.67 and RMSE = 855 pptv). CO is underpredicted in the PBL and UT but matches observations well in the free troposphere (*R* = 0.60 and RMSE = 22 ppbv). Observations in clear air at 12 km altitude show mean O₃ mixing ratio of 113 ppbv, which is higher than that predicted by WRF-Chem. This high O₃ could be a result of one of two phenomena that were occurring at the time. One phenomenon was potentially high O₃ in the UT anticyclone, which was primarily to the west of Mississippi, yet the 300 hPa analysis showed air from the outside the anticyclone region flowing to Mississippi (Figure S9). Ozone sonde data from both Houston and Smith Point (near Houston) show O₃ > 100 ppbv at 12 and 13 km, while the Huntsville, AL ozone sonde shows O₃ at ~75 ppbv. The second phenomenon is an intrusion of stratospheric O₃ (the tropopause altitude is ~14 km, Figure 5e) from an upper-level trough in the Northeast of the United States (Figure S9a). Figure S10 shows O₃-CO relationship for observations and modeling during the entire DC-8 flight. This tracer space diagram shows the relationship between the two tracers, one stratospheric and the other tropospheric in nature, similar to that described in Homeyer et al. (2014). The results are indicating that there is a relationship between O₃ and CO consistent with a clear O₃ stratospheric intrusion. It is important to note that these results are showing the high performance of the WRF-Chem initialized with CAM-Chem in representing the transitional air mass between the two branches. The UT anticyclone and/or the stratospheric O₃ contribution is not very clear in the observations, but further investigation of this phenomenon would go beyond the scope of this work.

4. Analysis Methods

4.1. Sample Determination of Inflow, Outflow, and BL

The first step in the observation analysis was to inspect each of the 2 September storm outflow intercepts to eliminate potential issues with data time-lags due to differences in the time response of the various instruments employed here. Although each individual DC-8 data point was appropriately time-shifted to a common time base, the analysis indicated residual differences in the measurements of a few seconds, which in some cases can impact the analysis due to the very short outflow intercept times. Rather than rely on one specific time for each outflow period for the gases studied here, we individually identified maximum or minimum concentrations in each outflow period. In the case of the trace gases, CO and CO₂ as well as CH₂O, SO₂, and CH₃OOH, the outflow intercepts clearly had higher mixing ratios than the UT background air. Their maximum values sometimes differed by several seconds, and our analysis employed the maximum concentrations for each individual species in the outflow periods. In the case of H₂O₂, the cloud outflow regions had lower mixing ratios than UT background air; thus, we used the minimum concentrations for our analysis. The next step was the identification of the inflow and outflow region and the verification of whether the outflow region intercepted by the aircraft corresponded to the air sampled in the inflow regions. As the SEs are defined as the amount of a soluble trace gas removed by a storm during the transport of a parcel of air from the inflow to the outflow regions, the accurate identification of coherently related inflow and outflow regions is important for accurate SE determinations (Fried et al., 2016).

Based upon the characteristics of the evolving storm using the radar reflectivity imagery and the geometric proximity of the outflow to the inflow region, it was determined that outflow intercepts 2–5 at 8 km height (Core 2) are coherently related to the boundary layer inflow labeled BL1, while Outflow Intercepts 11 and 14 (storm Core 7) are spatially closer to BL2 (Figure 1).

We estimated the time when the sampled air parcel would have been in the boundary layer. During convective PBL regimes as in this study, the cloud base is approximately the same as the PBL height. Although this is not a precise method, it is reasonable to state that air ingested in the cloud base comes from the PBL. Since the cloud base is in or at the top of the PBL, the time since cloud base was determined from aircraft measurements. The cloud base height ($z = 600$ m MSL) was found using MMS GPS altitude data from the aircraft ascent after BL1 inflow air was sampled. APR-2 vertical velocity vertical profiles for each cloud intercept showed that the updrafts averaged between 5 and 7 m s⁻¹ for both the airmass and multicell storms. Thus, calculations of time since cloud were computed for $w = 5$ and $w = 7$ m s⁻¹.

For Outflow Intercepts 2–5, the time since cloud base ranged from 18 to 25 min for $w = 7$ and 5 m s⁻¹, respectively, and the estimated time at cloud base was between 17:29 and 18:05 UTC, which is within an hour of the BL1 measurements (sampled at 16:53–16:54 UTC). For Outflow Intercepts 11 and 14, the time since cloud base was approximated as 27 and 38 min for $w = 7$ and 5 m s⁻¹, respectively, indicating that the time at cloud base was 18:53 and 19:41 UTC.

BL2 inflow was sampled at 22:12–22:18 UTC, which was >2 hr after Outflow Intercepts 11 and 14 were sampled, and ~3 hr after the intercepts air parcel was likely in the boundary layer. Thus, we employed the photochemical box model, BOXMOX (Knote et al., 2015), to estimate inflow mixing ratios of trace gases used in the analysis.

BOXMOX extends the Kinetic PreProcessor (KPP; Sandu & Sander, 2006) to give a user-friendly means of setting up the box model simulations. BOXMOX can be used to represent a plume (i.e., follow an air parcel), the PBL diurnal variation, or laboratory chamber conditions (Knote et al., 2015). Here, we use BOXMOX to represent the PBL diurnal variation configuration, which allows the box to grow and shrink in volume according to the PBL height, emissions, dry deposition, and exchange with the air above the PBL. The BOXMOX chemistry used here is the MOZART-T1 chemical mechanism (Emmons et al., 2020), which includes a more detailed description of the oxidation of isoprene and terpenes, organic nitrate speciation, and aromatic speciation and oxidation than its previous version MOZART-4. Initial concentrations were taken from the BL1 inflow measurements for trace gases that were measured. However, some species had to be estimated using guidance from the WRF-Chem simulation. CH₃OOH was initialized to 1 ppbv, glyoxal to 1 ppbv, methyl glyoxal to 200 pptv, glycolaldehyde to 500 pptv, formic acid to 500 pptv, and acetic acid to 200 pptv. Both anthropogenic and biogenic emissions were based on those used for the WRF-Chem

Table 1
Soluble Species Mixing Ratios (pptv) From Observations and WRF-Chem Simulations of the 2 September 2013, Airmass Storm Inflow/Outflow Regions

	CH ₂ O		H ₂ O ₂		CH ₃ OOH	
	Mean	SD	Mean	SD	Mean	SD
Avg. Intercept 2–5 inflow	5,480	216	2028	179	N/A	N/A
Avg. Intercept 2–5 outflow	1,589	257	309	85	N/A	N/A
WRF-Chem no scav.	1,208	365	2,304	697	647	156
<i>r_f</i> = 0.0	852	227	558	191	595	136
<i>r_f</i> = 0.3	667	150	244	293	595	130
<i>r_f</i> = 0.6	514	91	213	288	589	134
<i>r_f</i> = 1.0	396	55	200	279	576	128

simulations of the innermost domain. Temperature and the PBL height were prescribed in BOXMOX using values from the WRF-Chem simulation. Photolysis rates were obtained from the Tropospheric Ultraviolet Visible (TUV) radiation model (Madronich & Flocke, 1997) for the day and location of the region (32.5°N, 90.0°W) with output given for a 0.5 km altitude. The TUV photolysis rates were then scaled by a factor of 0.8 to match the BL1 measurements. Dry deposition of CO, O₃, NO, NO₂, NO₃, HNO₃, N₂O₅, HO₂NO₂, H₂O₂, CH₃OOH, and SO₂ were included. The region above the PBL was given the same initial concentrations as the PBL region to minimize effects of entrainment. BOXMOX began its simulation at 12 noon local time and was integrated for 12 hr.

The BOXMOX results agreed within the variability of the BL2 measurements for NO, NO₂, O₃, isoprene, ethylene, and propane. NO_y is under-predicted by a factor of 3.7, while H₂O₂ is over-predicted by a factor of

1.5. BOXMOX CH₂O mixing ratios capture the decrease from 12 noon (5.4 ppbv) to 17:15 local time (3.9 ppbv) seen in the measurements. Thus, we use BOXMOX CH₂O mixing ratios (4.5 ppbv) at 14:15 local time (19:15 UTC) as the inflow for the analysis of Outflow Intercepts 11 and 14. Since BOXMOX over-predicted H₂O₂, the inflow H₂O₂ mixing ratio for the analysis of intercepts 11 and 14 is set to 2.45 ppbv, which is interpolated from the BL1 and BL2 measurements of 2.028 and 2.795 ppbv, respectively. Recall that ratios of CH₃OOH to its standard are used for the observational analysis of CH₃OOH SEs (thus, its observed mixing ratio is not given). The peroxide mixing ratios employed in our analysis are listed in Tables 1 and 2. The mean inflow and outflow intercept mixing ratios are given in the first two rows of these tables, and the WRF-Chem simulations with no scavenging (no scav.) and with scavenging turned on employing different ice retention factors are given in the subsequent rows in both tables. Section 4.3 further discusses the WRF-Chem simulations. The 1σ standard deviations are given by the columns labeled SD.

4.2. SEs Determined From Observations

SEs can be determined using different approaches. Comparing the flux of soluble trace gases in rain at the surface to the flux of that trace gas entering the storm (Easter & Hales, 1983; Barth, Kim, Skamarock, et al., 2007) is a direct method that is challenging to observe, but easier to model if trace gas concentrations in rain are explicitly predicted. Comparing the ratio of a soluble trace gas to an insoluble, nonreacting (on the time scales of convective transport) trace gas in the outflow region to that ratio in the inflow region (e.g., Apel et al., 2012; Fried et al., 2016) is a simple approach that only accounts for entrainment at inflow and outflow altitudes. Using a multicomponent mixing model (Barth et al., 2016; Cohan et al., 1999; Fried et al., 2016; Yang et al., 2015), allows for entrainment at several altitudes to be included and is an appropriate method to use when analyzing observations. These various gas phase approaches can provide SEs over the inflow and outflow measurement time periods, but there remains the possibility that residual trace gases may evaporate from the condensed phase over longer time periods further downwind (Lawrence &

Crutzen, 1998), thus resulting in overestimates for the SEs. In addition, evaporation of precipitation below cloud can also occur allowing dissolved trace gases to return to the gas phase, and thus redistribute the trace gas rather than remove it from the atmosphere. Our observational analysis does not account for the possibility of below-cloud analysis because we essentially calculate a transport efficiency and assume the remainder is removed. This approach could be an issue for the case of moderately soluble gases like CH₂O. However, the small prefrontal convection studied here developed in light (<5 m s⁻¹) southerly winds from the Gulf of Mexico with relative humidity >80% below cloud base (Figure S8). Thus, we do not expect substantial evaporation below cloud for this case. From the modeling perspective, the WRF-Chem wet scavenging parameterization accounts for evaporation, allowing trace gases to redistribute vertically.

Table 2
Soluble Species Mixing Ratios (pptv) From Observations and WRF-Chem Simulations of the 2 September 2013, Multicellular Storm Inflow/Outflow Regions

	CH ₂ O		H ₂ O ₂		CH ₃ OOH	
	Mean	SD	Mean	SD	Mean	SD
Avg. Intercept 11 and 14 inflow	4,500	-	2,450	-	N/A	N/A
Avg. Intercept 11 and 14 outflow	993	134	286	-	N/A	N/A
WRF-Chem no scav.	987	457	1,580	697	374	177
<i>r_f</i> = 0.0	717	283	389	69	344	159
<i>r_f</i> = 0.3	326	33	130	163	344	158
<i>r_f</i> = 0.6	194	44	113	66	335	153
<i>r_f</i> = 1.0	153	65	105	168	315	140

Following the analysis of Fried et al. (2016) and Barth et al. (2016) for analyses of DC3 storm cases, we employ here two methods for calculating the dilution of various trace gases due to lateral entrainment of background air into the convective core during transport from the inflow to the outflow region. The first method employs measurements of the non-soluble tracers, CO and CO₂, in determining a column-averaged entrainment rate, α . We denote this as the Constant Column Entrainment (CCE) method. The CO₂ tracer was used with caution to ensure that no photosynthetic uptake from the biosphere comes into play. Fortunately, this effect is fairly obvious, as significantly reduced CO₂ levels are observed due to uptake by photosynthesis, in contrast to elevated levels in the convective outflow in the absence of this effect. As discussed in Fried et al. (2016), the tracer concentration in each 1-km altitude bin (X_i , where i is the altitude bin) is calculated in accordance with:

$$X_i = (1 - \alpha)X_{(i-1)} + \alpha X_{(BKG)i}, \quad (1)$$

where $X_{(BKG)i}$ is the measured tracer background concentration in the i th altitude bin, determined from the median Clear Air (CA) aircraft tracer concentrations discussed previously at each 1-km altitude bin.

The value of α for each tracer is determined in an iterative fashion to match the calculated tracer concentration at the sampled outflow altitude ($X_{calc, OF}$) with that measured in the convective outflow. When CO₂ measurements can be employed, we determine the column-averaged entrainment rate α and its standard deviation using both CO₂ and CO. Using this column-averaged entrainment rate value, the soluble gas outflow concentration (Y_i) at each 1-km altitude step is then calculated in a similar fashion as equation 1, in accordance with

$$Y_i = (1 - \alpha)Y_{(i-1)} + \alpha Y_{(BKG)i} = Y_{calc, OF}. \quad (2)$$

At the outflow altitude, the calculated soluble tracer ($Y_{calc, OF}$) from equation 2 is determined. This mixing ratio, $Y_{calc, OF}$ represents the soluble species Y diluted by entrainment but not scavenged in the storm.

The second method finds different entrainment rates for each 1-km altitude based on WRF-Tracer simulations (Bela et al., 2016, 2018) to provide additional support to our first method. We denote this method as the Variable WRF-Tracer Entrainment (VWE) method. This modeled altitude-dependent tracer method relies on the highest resolution model domain (1.35 km horizontal resolution) using artificial model tracers assigned to each 1-km altitude bin from the ground level up to 15 km above ground level (a.g.l.) just before the convective initiation of each selected simulated cloud. The simulation of tracer transport is 50 min long. The modeled outflow region is then analyzed to determine the contribution of the released tracer from each 1-km altitude layer to the outflow region. This methodology allows the determination of variable entrainment rates at each altitude, and equation 2 is thus modified with this variable entrainment rate at each 1-km altitude step in determining the calculated concentration of soluble species Y diluted by entrainment. Upper and lower limits to these values are also determined in both approaches from the appropriate standard deviations. For comparison purposes with the first method, we also calculate the column-averaged entrainment rate from the VWE method. However, for the SE calculations using the VWE method, the variable entrainment rates are employed.

Finally, as in Fried et al. (2016), the SE was then determined by comparing the $Y_{calc, OF}$ value with that measured in the outflow (Y_{meas}) from

$$SE = (Y_{calc, OF} - Y_{meas}) / Y_{calc, OF}. \quad (3)$$

The final value of SE for every cloud outflow intercept employs the average of the SE calculations using both (observed tracer and Variable WRF-tracer) entrainment rate methods.

4.3. SEs Determined from WRF-Chem Simulation

Microphysical scavenging is one of the dominant removal processes of the species studied in this work (Bela et al., 2016, 2018). The wet scavenging parameterization used in our study is based on Neu and Prather (2012), which is described in more detail by Bela et al. (2018). The scavenging amount calculated for a given species depends upon the net precipitation production rate ($precip - kg\ kg^{-1}\ s^{-1}$) of rain, snow, and graupel

from cloud water and ice (*rainprod*) minus evaporation (*evapprod*) at each model level (*z*) during a time step (Δt , s):

$$precip(z) = \{rainprod(z) - evapprod(z)\} \Delta t. \quad (4)$$

The overall WRF-Chem SE is then related to 4 terms according to

$$SE \propto \sum_{z=Z_{CB}}^{z=-15^{\circ}C} \{rf\} \{H_{eff}(z)\} \{A_g(z)\} \{precip(z)\}. \quad (5)$$

Thus, the SE is proportional to the product of the *rf*, the effective Henry's Law value (H_{eff} , mol-L⁻¹ atm⁻¹), the gas phase mixing ratio (A_g , ppbv), and the net precipitation production rate. Here, the summation is from the cloud base height (ZCB) to the height where $T = -15^{\circ}C$, because the WRF-Chem wet scavenging scheme operates only for $T > -15^{\circ}C$ for trace gases other than HNO₃. We have not tested the effect of the $T > -15^{\circ}C$ bound on the WRF-Chem results.

An important quantity in the wet scavenging code is the *rf* value that defines the fraction of the simulated species retained in ice in the mixed phase of the storm (i.e., $-15^{\circ}C < T < 0^{\circ}C$). The *rf* value is a prescribed parameter in the code and has different values for each species. The WRF-Chem SE calculations start with *rf* values prescribed of 0.64 for CH₂O and H₂O₂ and 0.02 for CH₃OOH, and these values are then adjusted in the simulations such that the calculated WRF-Chem SEs match the values determined from the observations previously discussed.

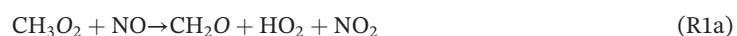
To determine the WRF-Chem SE, two simulations were conducted, one with wet scavenging and one without wet scavenging. The SE is then determined as follows:

$$SE(\%) = 100 \times \left(\frac{q_{i,noscav} - q_{i,scav}}{q_{i,noscav}} \right), \quad (6)$$

where $q_{i,noscav}$ and $q_{i,scav}$ are the mean outflow mixing ratios of species *i* in the simulation without wet scavenging and a simulation with wet scavenging turned on, respectively. Figure S11 presents an example of the absolute difference in CH₂O mixing ratios of one selected simulated cloud when the wet scavenging scheme in the WRF-Chem model is turned on and off.

4.4. SE Corrections From Enhanced NO

The Outflow Intercepts 11 and 14 (Core 7) provide an additional challenge in our SE analysis. Not unlike many other studies, these intercepts experienced very high NO levels approaching 2 ppb, most likely from lightning. We address in this section the influence that this may have on the SEs for CH₂O, H₂O₂, and CH₃OOH. In the case of CH₂O, enhanced NO may lead to enhanced production of CH₂O in the presence of O₂ from (R_{1a}):



Since R_{1a} competes with R_{1b}, such enhanced NO would also reduce the production of CH₃OOH. Likewise, such enhanced NO would also depress the production of H₂O₂ via R₂ since R₃ would dominate:



If not corrected, the production of CH₂O would yield an erroneously low SE. By contrast, the depression in the peroxides would result in erroneously high SEs.

We determined the NO production correction factor for CH₂O and the depression for H₂O₂ based on two methods one estimated from observations and the other with the aid of a parcel model. Figure 5 shows the cloud Outflow Intercept 14 (Core 7) temporal profiles for CH₂O (purple lines), CO (black lines), NO

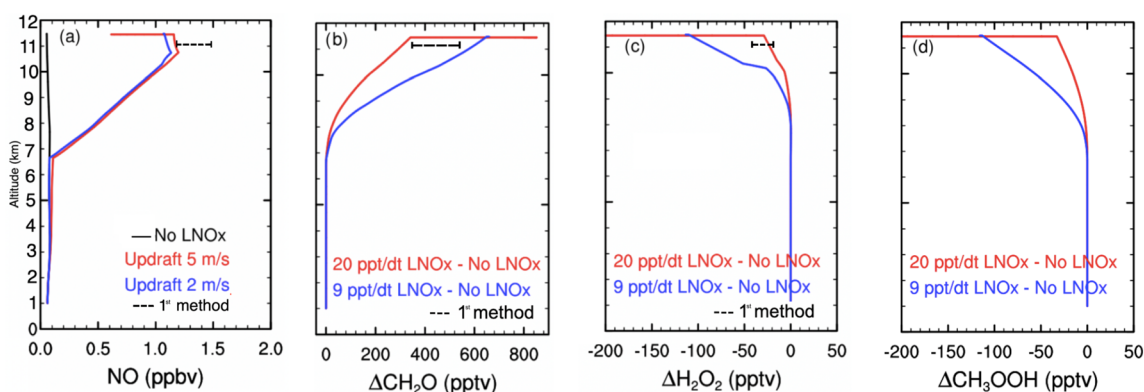


Figure 6. Parcel model vertical profile of results for (a) NO, (b) $\Delta\text{CH}_2\text{O}$, (c) $\Delta\text{H}_2\text{O}_2$, and (d) $\Delta\text{CH}_3\text{OOH}$ for simulations with no LNO (black lines), and with LNO of 20 pptv NO per 10-second time step (red lines) and 9 pptv NO per 10-second time step (blue lines) to produce 1–1.47 ppbv of NO. Panels (b)–(d) show the difference between the simulations with LNO and without LNO, and Panels (a), (b), and (c) also show results from the first method (dashed black line).

(red lines), and H_2O_2 (green points with lines). This figure provides the rationale for the first method. The shaded region for this cloud intercept depicts the portion of the outflow where CO is constant, and hence any changes in CH_2O and H_2O_2 due to NO can be ascribed to chemistry and not changes in dilution. Intercept 11 produced similar temporal profiles. Thus, the CH_2O production rate was determined from the linear regression slope of CH_2O as a function of NO for the combined data set (451 ± 35 pptv/ppb). The H_2O_2 regression slope vs NO for Intercept 14 (no H_2O_2 data for Intercept 11) for these same points yielded a value of -32 ± 6 pptv/ppb. These slopes ($d\text{CH}_2\text{O}/d\text{NO}$) and ($d\text{H}_2\text{O}_2/d\text{NO}$) were then multiplied by the average of the two median NO concentrations in the outflow plumes (1.367 ± 0.145 ppb) minus the average NO in the cloud free background air at this altitude (0.358 ± 0.150 ppb). This resulted in an estimated CH_2O production of 455 ± 101 pptv due to NO, and a H_2O_2 depression of 32 ± 9 pptv. We do not have results here from this first method for CH_3OOH since we do not have absolute CH_3OOH mixing ratios.

The second method employed in estimating the effects of enhanced NO was a parcel model described in Barth et al. (2016). This parcel model was used instead of BOXMOX because the Barth model represents both gas and aqueous phase chemistry while BOXMOX does not, and the Barth model easily works with changing air density as the parcel is lifted, while BOXMOX uses a fixed air density. The 1 to 1.4 ppb average enhanced NO observed in Figure 5 was used to approximate one of the end points in this model. This parcel model was run with two different assumed emission profiles for lightning-produced NO (LNO), that is, 20 and 9 pptv per 10-s time step. As it is not possible to know the exact exposure time to enhanced NO, these calculations are meant to serve as potential indicators as to what may happen to various trace gases in convection in the presence of lightning, and thus as a validation to the results of the first method. Figure 6 shows the (a) two NO-enhancement scenarios and the resulting modeled production/depression rates of (b) CH_2O , (c) H_2O_2 , and (d) CH_3OOH . This modeling exercise yields enhanced CH_2O of 310 to 610 pptv, reduced CH_3OOH and H_2O_2 production in the 30 to 110 pptv range, and no effect on SO_2 . Note that the effect on $\text{HOCH}_2\text{O}_2\text{H}$ was not estimated here as its chemistry is not included in the parcel model. It is interesting to note that the midpoint for the CH_2O parcel model production estimate (460 pptv) almost exactly falls on our first estimate of 455 pptv. The lower H_2O_2 depression estimate of 30 pptv is also close to our first estimate of 32 pptv, but the midpoint (70 pptv) is higher than our observational estimate.

5. Results

5.1. SEs Derived From Observations

The average entrainment rate per kilometer ($\% \text{ km}^{-1}$) when employing the CCE method using CO and CO_2 observations yielded $\alpha = 11.4 \pm 1.6\% \text{ km}^{-1}$ ($N = 4$) and $\alpha = 8.3 \pm 1.6\% \text{ km}^{-1}$ ($N = 2$), for intercepts in the airmass storm (Core 2) and multicellular storm (Core 7), respectively. These values are in reasonable agreement with the VWE method results of $9.0 \pm 6.3\% \text{ km}^{-1}$ for the airmass Core C and $8.0 \pm 15.6\% \text{ km}^{-1}$ for the

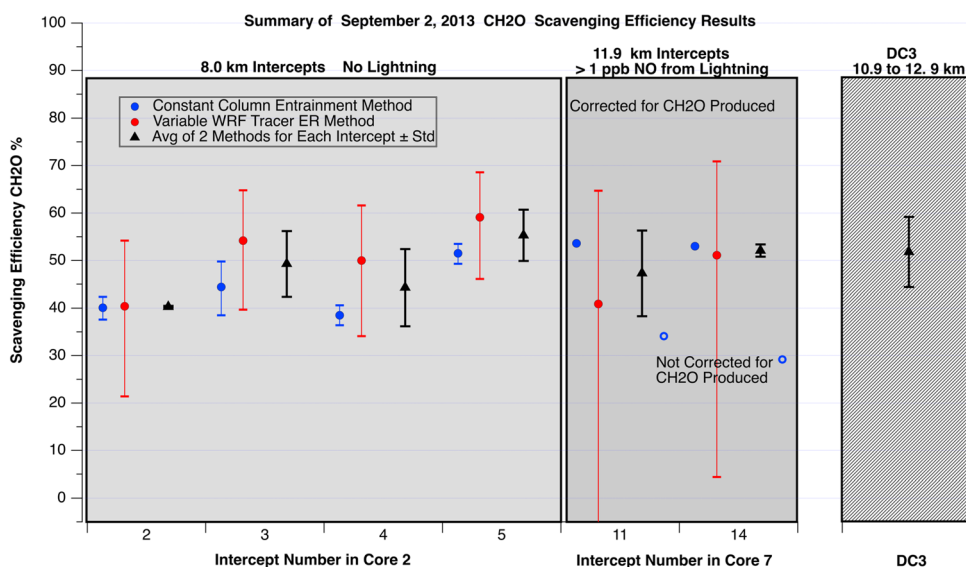


Figure 7. CH₂O SEs for intercepts in air mass storm Core 2 (left panel) and in multicellular storm Core 7 (middle panel) using the CCE method (blue markers), variable WRF method (red markers), and average of these two methods (black markers). Open blue circles in the middle panel show the SEs when CH₂O mixing ratios are not corrected for LNO effects. The average and standard deviation from six DC3 storms (right panel) are also shown.

multicellular storm Core A. Table S5 provides the entrainment rates for each 1-km altitude layer based on the VWE method simulation.

Figure 7 provides CH₂O SE results using the CCE method and the variable WRF method as well as the average of these two methods for each cloud outflow intercept. The error bars on each result represent the SE lower and upper bounds determined by the standard deviations of the entrainment rates. Despite the fact that the WRF tracer simulations have rather large error bars due to large variations on the individual altitude dependent entrainment rates (see Figure 5c), the VWE method average SE values for each intercept are close to those from the CCE method and the average values of the two methods are therefore used in the analysis. The average CH₂O SE for Core 2 over the four intercepts (2 to 5) yields an average SE = $47 \pm 8\%$ ($N = 8$) and for Core 7 over two intercepts (11 and 14) yields an average SE = $50 \pm 6\%$ ($N = 4$), after correcting for lightning enhancements in the CH₂O production. The number in the SEs in the averages treats the constant and variable entrainment values as separate, and hence there are eight individual determinations for Core 2 and four for Core 7. The composite SE average for CH₂O for all the intercepts of Figure 7 is $48 \pm 7\%$ ($N = 12$). It should be noted that this composite average for 2 September 2013 is equivalent within the uncertainty limits to the DC3 values of ($SE = 52 \pm 7\%$) at 10.9 to 12.9 km for more severe convection (right panel of Figure 7 and Fried et al., 2016).

While the CH₂O SE for the multicellular storm is $47 \pm 8\%$ when correcting for lightning-production of NO, it is $36 \pm 7\%$ without correcting for lightning-production of NO (Figure 7). The correction from lightning-generated NO in CH₂O SE was from two approaches that estimated CH₂O production consistently. However, it is important to mention that one cannot a priori assume such enhancements in all cases, since many factors are important, including NO exposure times, injection altitudes and VOC levels, to name a few.

Figure 8 displays resulting SEs for H₂O₂, HOCH₂O₂H, CH₃OOH, and SO₂, in a similar fashion as CH₂O SE in Figure 7 for both Core 2 and Core 7, but displaying the average SE for the two entrainment rate methods only. The H₂O₂ SEs, which range between ~80 and 90% in the two different storm types (overall average = $83 \pm 4\%$, $n = 10$) are very similar to that determined during DC3 (right panel of Figure 8). On the other hand, the CH₃OOH SEs show lower values (4–27%) than the SEs determined from DC3 storms (12% to 84%, for 6 cases of mostly severe thunderstorms—Figure S12). While the potential bias in CH₃OOH data is applicable to both DC3 and SEAC⁴RS data, other differences between DC3 and SEAC⁴RS CH₃OOH data should not introduce a greater bias in DC3 results than SEAC⁴RS results. The lower CH₃OOH SEs found for SEAC⁴RS are more in line with that expected based upon CH₃OOH low solubility.

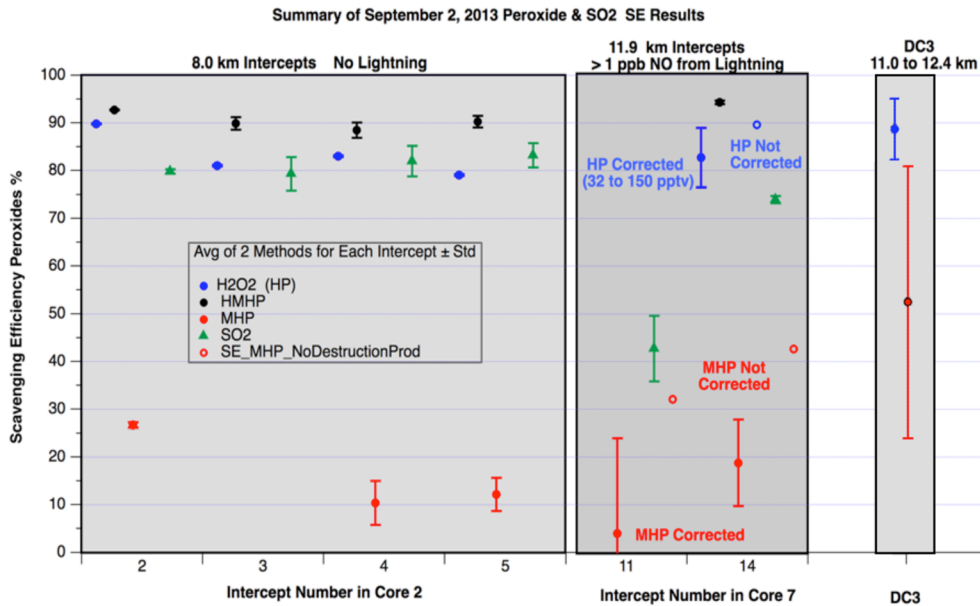


Figure 8. As in Figure 8 but for the H₂O₂, HOCH₂O₂H, CH₃OOH, and SO₂. The error bar on the LNO corrected H₂O₂ reflects the 32–150 pptv range of the correction. The CH₃OOH error bars indicate the standard deviations of the two entrainment rate methods. Note that Intercept 3 has missing CH₃OOH data, and Intercept 11 has missing H₂O₂ and HOCH₂O₂H data.

The HOCH₂O₂H SEs revealed high values ranging between 89% and 94% for both Cores 2 and 7. These high SEs for HOCH₂O₂H are expected based on the high solubility of HOCH₂O₂H. The SO₂ SE values present different ranges depending on the storm. The SO₂ SE averages $81 \pm 3\%$ ($N = 8$) for Core 2 but averages $58 \pm 19\%$ ($N = 4$) for Core 7. These SO₂ SEs are similar to higher in magnitude than previous studies (Mari et al., 2000; Barth, Kim, Skamarock, et al., 2007).

5.2. WRF-Chem Predicted SEs

As shown in section 5.2, the WRF-Chem simulation represented the characteristics of the observed clouds. By conducting several sensitivity simulations each with different ice retention factors, the *rf* values can be estimated by finding the best agreement between SEs calculated from observations to the SEs simulated by WRF-Chem. The SEs determined by the WRF-Chem results can be plotted against the *rf* used for that simulation (Figure 9). There are two important results shown in Figure 9: (1) there is a large range of *rf*

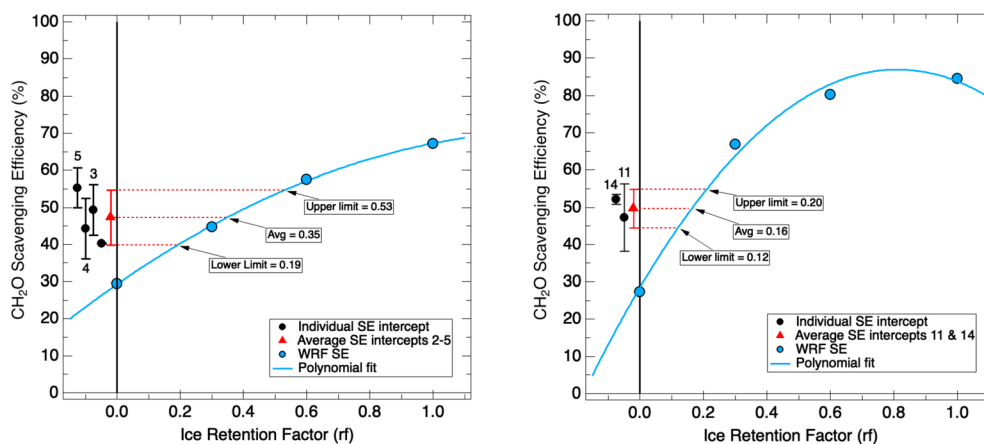


Figure 9. WRF-Chem CH₂O SEs (dots) for different *rf* from simulations of selected (a) airmass and (b) multicellular simulated clouds, and individual intercept SEs observed (black dots) and the average values for each core (red triangles).

values that match the SE observations within the measurement uncertainty limits, and (2) the rf range is highly nonlinear. In the case of CH_2O , rf values of 0.2 to 0.5 and 0.1 to 0.2, match the observations for the airmass (Figure 9a) and multicellular (Figure 9b) storms, respectively. The WRF-Chem simulations showed a 5–7% effect CH_2O SEs caused by lightning- NO_x emissions and subsequent chemistry for the multicellular storm, suggesting the rf value may have a slightly wider range. The rf values of 0.2 to 0.5 (average value of 0.35) determined here for CH_2O for the airmass and 0.1 to 0.2 (average value = 0.16) for the multicellular storms are similar to rf values <0.25 determined by Bela et al. (2018) for two DC3 storms with more severe convection than investigated here. Bela et al. (2018) estimated $rf = 0.25$ for the Alabama airmass storm, which agrees with our findings for the SEAC⁴RS airmass storm.

Our WRF-Chem rf analysis further reveals that the WRF-Chem calculations are highly sensitive to the precise convective core selected in the simulations to match the observed convection. Even using a high-resolution ($\Delta x = 1.35$ km) WRF-Chem simulation in this case study, we still encountered uncertainties in the simulations due to the natural small, subgrid-scale characteristics of the observed clouds. Hence, the storm outflow regions represented in the model have only a small number of grid cells (in this case, 12 and 9 grid cells in the simulation of the multicellular and airmass storm, respectively), some of which may also include air entrained from outside the outflow region because these grid cells are located at the edges of the storm. In addition, ice-phase and liquid-phase processes are complex parameters not only to measure but also to simulate due to the wide variety of particle types making difficult the quantification of uncertainties. Thus, despite the ability of regional models such as WRF-Chem to represent mesoscale motions in convection producing reasonable storm structures, the uncertainties in the cloud physics processes and IWC, in particular, make it challenging to select a precise outflow region in the simulations, which increases the uncertainties in the rf estimation.

For H_2O_2 , in contrast to CH_2O , the SE- rf plot is rather flat, showing very little change in the WRF-Chem calculated SE for a wide range of rf values. We calculate rf values between 0.1 and 0.4 to best match the SE observations in the 80 to 90% range, and this result overlaps with the $rf < 0.25$ estimated for the DC3 storms simulated by Bela et al. (2018). The WRF-Chem simulations showed $\sim 1\%$ effect on H_2O_2 SE caused by lightning- NO_x and subsequent chemistry. Ice retention values much higher than this results in SEs of $\sim 92\%$ and $\sim 90\%$ for multicellular and airmass storms, respectively, and a value of 0 only reduces the calculated SE results to 75% and 76% for multicellular and airmass storms, respectively.

For both SEAC⁴RS storms studied here, the CH_3OOH SEs were not sensitive to the tested range of rf . These results are in contrast with Bela et al. (2018) who showed CH_3OOH SEs were sensitive to rf for DC3 storms. Effects of lightning- NO_x and subsequent chemistry in the WRF-Chem simulations are small ($\sim 2\%$ change in CH_3OOH SE). Finally, no rf values were derived for $\text{HOCH}_2\text{O}_2\text{H}$, which is not part of the chemical mechanism in WRF-Chem, or SO_2 since our WRF-Chem simulations did not include aqueous chemistry, which prevented further analysis of this gas.

5.3. Discussion

The interaction between the simulated cloud microphysics and the scavenging of species is made through the analysis of in-cloud (i.e., $\text{QCLOUD} > 0.00001$ g kg^{-1}) vertical profiles of hydrometeors (Figure 10a), SEAC⁴RS and DC3 net precipitation production (Figure 10b), and in cloud gas-phase mixing ratios with scavenging scheme in WRF-Chem for CH_2O , H_2O_2 , and CH_3OOH for cloud Core A (Figures 11c–11e, respectively). The two storm cores show similar vertical structure for hydrometeors (Figure 10a) and net precipitation production (Figure 10b), and this is also true for almost all simulated clouds that were analyzed (not shown). The results show that cloud water is the dominant hydrometeor at $z < 6$ km, while graupel has the highest concentration at the levels where the DC-8 intercepted the observed clouds. The cloud water mixing ratios are comparable to those simulated for the severe DC3 convection as well as the MCS analyzed by Bela et al. (2018). While hydrometeors show the microphysical structure of the simulated cloud, the net precipitation production is the controlling variable that one can use to explain differences in rf . The average and the sum of the net precipitation production rate over 50 min of the storm development are presented in Figure 10b along with the mixed-phase region between -15°C and 0°C where most of the supercooled cloud drops are located. It is the altitude range of this region and the net precipitation production rate values that determine the net amount of soluble species that can reach the freezing level where ice is formed. The

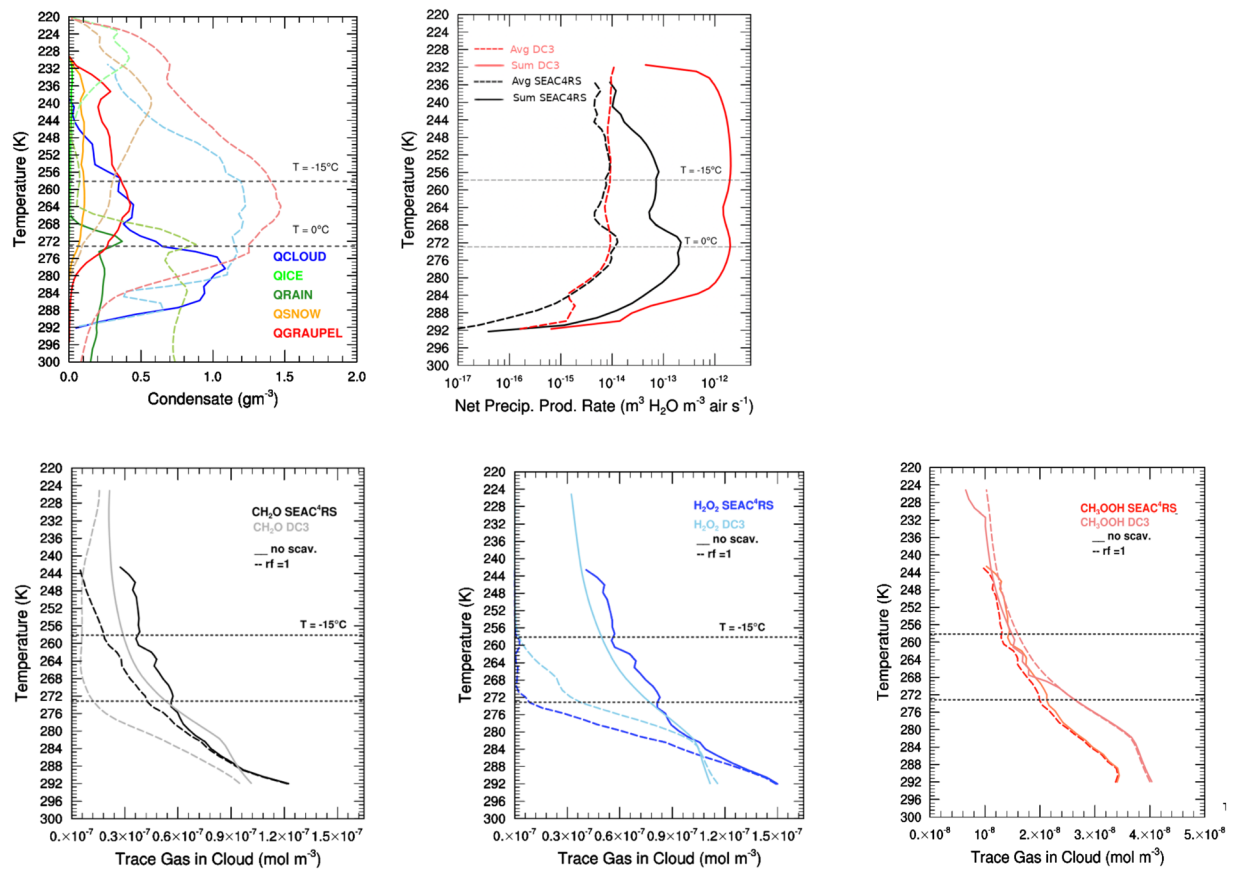


Figure 10. Simulated (a) hydrometeors, (b) net precipitation production rate, and in-cloud gas-phase mixing ratios of (c) CH₂O, (d) H₂O₂, and (e) CH₃OOH within the multicell storm (WRF cloud core A). In (a), solid lines are for the SEAC⁴RS storm cores while dashed lines are for the 29 May 2012 DC3 severe storm. In (b), black lines are for the SEAC⁴RS storm cores while red lines are for the DC3 severe storm. In (c), dark lines are for the SEAC⁴RS storm cores with (dashed line, using $rf = 1$) and without (solid) scavenging scheme on, and light lines are for the DC3 severe storm with and without scavenging scheme on.

highest simulated net precipitation production occurs in this interface region between the warm- and mixed-phase of the cloud (~5–7 km height) with average values up to $1.2 \times 10^{-14} \text{ m}^3 \text{ H}_2\text{O m}^{-3} \text{ s}^{-1} \text{ air}$ for the multicellular storm and up to $0.5 \times 10^{-14} \text{ m}^3 \text{ H}_2\text{O m}^{-3} \text{ s}^{-1} \text{ air}$ for the airmass storm (not shown). In the case of the very soluble H₂O₂, very little gas phase H₂O₂ enters the mixed-phase regions of both storms (Figure 10d), which is very similar to the more severe convective cases discussed by Bela et al. (2018). This can be clearly seen by the very steep drop in the gas-phase H₂O₂ levels entering the mixed-phase region, in contrast to CH₂O (Figure 10c) and CH₃OOH (Figure 10e).

Although the SEAC⁴RS storm SEs for H₂O₂ (high solubility) and CH₂O (moderate solubility) are remarkably consistent with the DC3 results, these results show that there is a difference in the region of the cloud where the highest amount of soluble species was removed for these two species. While SEAC⁴RS H₂O₂ was rapidly depleted in the warm phase of the cloud (Figure 10d), the severe storm studied in DC3 allowed the fast depletion of both H₂O₂ and CH₂O in the warm phase of the storm, with a consequence that more CH₂O like H₂O₂ was removed before entering this mixed-phase region. In the case of CH₂O, there is a significant difference in the vertical structure in the observed mixing ratios between the DC3 storms and the two storms studied here. During DC3, the severe storm case on 29 May 2012 had peak vertical velocities ranging between 20 and 60 m s⁻¹ (Digangi et al., 2016), and it is more severe to the SEAC⁴RS storms presented in this work with average updraft velocities ranging between 2 and 4 m s⁻¹. The resulting reduced mass of gas-phase species entering the mixed-phase region in the case of H₂O₂ and CH₂O for the severe DC3 storm case resulted in very low ice retention factors <0.25, and in the case of CH₂O, only a very narrow range of rf that satisfy the observations. This is in contrast to the wider range of rf values in in the SEAC⁴RS case (Figure 10) that match the

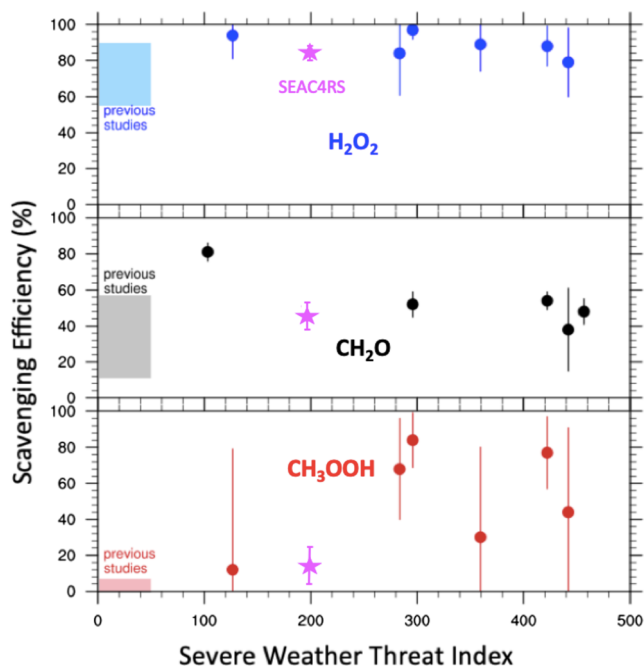


Figure 11. Scavenging efficiency versus severe weather threat index for SEAC⁴RS storms (magenta markers), DC3 storms (blue, black, and red markers) and previous studies (gray shading). Note that the previous studies did not identify the severity of convection.

species such as CH₃OOH. This effect becomes more evident when we plot SEs results from previous studies and the present study and plot them as a function of a weather index such as the Severe Weather Threat (SWEAT; Figure 11).

Previous laboratory and modeling studies SE values are presented in shaded rectangles, DC3 storms in dots, and SEAC⁴RS in stars. The species are organized based on its solubility, that is, the most soluble species H₂O₂ is presented in the upper panel, the moderate soluble gas CH₂O in the middle panel, and the least soluble gas CH₃OOH in the lower panel. The SWEAT Index evaluates the potential for severe weather by combining several parameters into one index including low-level moisture (850 hPa dewpoint temperature), instability (Total Totals Index), lower and middle-level (850 and 500 hPa) wind speeds, and warm air advection (veering between 850 and 500 hPa). Values ranging from 150 to 300, as the storm studied in this work and two storms in DC3, indicate slightly severe thunderstorms, and values ranging from 300 to 400 can represent a possible severe thunderstorm, and >400 a tornadic thunderstorm is possible.

6. Conclusions

In this work, observation and modeling techniques are combined to study vertical transport, entrainment rates, SE, and ice retention factors (*rf*) of soluble trace gases in convective storms using a case study that occurred on 2 September 2013 during the SEAC⁴RS campaign. The unique measurements of this case's convection properties and chemical composition enabled the quantification and analysis of storm processes impacting soluble trace gases, such as formaldehyde (CH₂O), hydrogen peroxide (H₂O₂), methyl hydrogen peroxide (CH₃OOH), hydroxy methyl hydrogen peroxide (HOCH₂O₂H), and sulfur dioxide (SO₂). Formaldehyde and the peroxides are important precursors for HO_x radicals and therefore O₃.

To determine SEs, the lateral entrainment of background air into the convective core must be determined. This study employed two methods to derive entrainment rates. One method used observed nonsoluble and nonreactive (on the time scales of convective transport) trace gases (CO and CO₂) while the second method used the WRF model and inert tracers. The WRF-tracer and WRF-Chem simulations satisfactorily represented small-scale convective storms, thus proving to be a useful tool for entrainment rate estimations to support observational analyses. Therefore, the SE for each cloud outflow intercept is calculated using both

observations. Thus, in addition to the three sources of uncertainty in determining *rf* values, particularly in the case of CH₂O previously discussed, the contrasting behavior between the SEAC⁴RS storms studied here and the severe DC3 storm case highlights the fact that, unlike the rather consistent SE results, there is not a single *rf* for CH₂O for each and every storm. Rather, the *rf* value will depend upon the particular storm dynamics, as more severe storms have more wet growth riming and turbulent conditions, which promote ice splintering and drop shedding. These processes can therefore affect the dissolved trace gases. Thus, different storm dynamics may explain the widely varying *rf* values for CH₂O deduced in previous studies: *rf* around 0 in Fried et al. (2016) Bela et al. (2016, 2018), *rf* = 0.64 in the wind tunnel experiment study by von Blohn et al. (2011), and the high value of 0.97 found in Jost et al. (2017) who studied dry growth riming process only.

The H₂O₂ *rf* values between 0.1 and 0.4 of this study are consistent with the value <0.25 found in Barth et al. (2016) and Bela et al. (2016, 2018), but is significantly lower than the estimated value of 0.64 by von Blohn et al. (2011). The CH₃OOH SEs were not sensitive to the entire range of *rf* values. This is in direct contrast to the behavior found by Bela et al. (2018) for the DC3 storms where the simulated SE was more sensitive to the *rf* value, suggesting that ice retention is a significant component for the removal of CH₃OOH.

These results further suggest that the severity of the convection can play a role in the efficiency of removal in storm clouds of low solubility trace gas

entrainment rate calculation approaches. While the CH_2O overall average SE and H_2O_2 SE determined from observations are remarkably consistent with our previous DC3 results (Barth et al., 2016; Fried et al., 2016), CH_3OOH SEs results showed lower values than the SEs determined in DC3. The calculated SE averages for SO_2 (70–80%) were similar to previous studies. The $\text{HOCH}_2\text{O}_2\text{H}$ SE (>89%), determined for the first time from observations, is as expected from a highly soluble trace gas. A unique aspect of this analysis was the determination of the effect of lightning-produced NO on CH_2O and peroxides using both observations and a parcel model. In this study, we calculated corrections to the SEs, which are necessary to account for the chemical production of CH_2O and the destruction of peroxides resulting from lightning-produced NO, which had mixing ratios up to 2 ppbv. Thus, we recommend that future analyses of SEs consider the possible production of CH_2O and reduction of peroxides due to the production of lightning NO.

The WRF-Chem model results provided the ability to examine the role of ice retention in freezing drops via an ice retention factor (rf) by conducting sensitivity simulations with different values of the model prescribed rf values. In order to match the WRF-Chem SEs with those calculated from observations, rf values of 0.2 to 0.5 and 0.1 to 0.2 for CH_2O in the airmass and multicellular storm, respectively, and 0.1 to 0.4 for H_2O_2 were needed, while CH_3OOH SE was not sensitive to the prescribed rf . The CH_3OOH rf results differ from the rf values determined for DC3 storms, in which Bela et al. (2018) found a strong dependence of CH_3OOH SE on rf .

The overall differences between SEAC⁴RS and DC3 storms suggest that retention of dissolved trace gases in frozen precipitation seems to be more important for moderately soluble trace gases and that rf may be dependent on the type of storm or stage of storm development. In all the WRF-Chem simulations presented here and the ones described in Bela et al. (2018), highly soluble H_2O_2 is shown to be mostly depleted between cloud base and the freezing level (i.e., the warm region of the storm), while moderately soluble CH_2O is depleted in the warm region of the storm in the most severe storms of DC3 but not in the weaker airmass or multicellular storms. We believe the larger depletion in severe storms is due to higher precipitation production in the warm region (including the formation of hail) in severe convection compared to smaller storms. Thus, ice retention factors for CH_2O are most important for storms with modest updrafts (5–15 m/s), which are typical for not only midlatitude airmass storms but also tropical convection. The mildly soluble CH_3OOH also shows more depletion in the warm region of the storm for severe convection, but not nearly to the extent of CH_2O or H_2O_2 . While CH_3OOH scavenging may or may not depend on ice retention factors, other uncertainties, for example, entrainment (Bela et al., 2018) can affect the predicted SE.

While the SEs for CH_2O are remarkably similar in the SEAC⁴RS airmass and multicellular storms with those from the severe DC3 convective cases, chemistry transport models commonly employ Henry's Law values together with parameterized ice retention factors when calculating the effects of convective transport on UT O_3 rather than SEs. Although we arrived at consistent ice retention factors for the multicellular storm case and the severe DC3 storms, and in the process uncovered sources of uncertainty in their determination, there remain additional unresolved differences among CH_2O ice retention factors for the airmass storms studied here, the three-dimensional cloud-resolving study of Leriche et al. (2013), and the high value of 0.97 found in the wind tunnel studies of Jost et al. (2017). Thus, we recommend further investigations of (1) the sensitivity of modeled O_3 mixing ratios arising from convective transport due to differences in CH_2O ice retention factors arising from convective transport; (2) effects of specific cloud physics processes, especially the role of hail below the freezing level, in affecting on CH_2O ice retention factors; and (3) the role if any on the specific type of freezing (homogeneous vs heterogeneous) and turbulence in affecting ice retention factors. In addition, future simulations should consider a sensitivity analysis for different cloud physics schemes to assess the impact of different parameterizations on SE calculations.

In summary, the present study extends our understanding of the vertical transport of O_3 precursors in various convective storm cases. Yet, the complex interactions between cloud microphysics and scavenging processes in convective clouds require additional studies to obtain observational data sets and studies in different types and stages of development of convective storms to advance our understanding even further. Special attention should be given to the location of various water hydrometeor phases within a cloud and their interaction with gases of different solubilities. Obtaining more composition measurements at a series of altitudes in the storm convective cores would be especially valuable to learn how much of the soluble trace gases are removed in the warm regions compared to the mixed-phase regions of the storms.

Acknowledgments

We would like to thank NASA for supporting this research through grant NNX17AH52G. NCAR is sponsored by the National Science Foundation. C. Homeyer was funded by NSF grant AGS-1522910. The authors thank Gabriele Pfister for providing additional WRF-Chem information. The authors also thank Morgan Silverman and Gao Chen for providing SEAC⁴RS formaldehyde comparison. We also thank NASA for supporting the SEAC⁴RS campaign, the project leaders, and all the investigators for their data contributions. All data were obtained from the NASA Langley Research Center Atmospheric Science Data Center (<https://www-air.larc.nasa.gov/cgi-bin/ArcView/seac4rs>). We acknowledge use of the WRF-Chem preprocessor tool (mozbc, fire_emiss, and bio_emiss) provided by the Atmospheric Chemistry Observations and Modeling Lab (ACOM) of NCAR and also the use of BOXMOX model provided by the University of Munich, Germany (<http://boxmodeling.meteo.physik.uni-muenchen.de>). Simone Tanelli's contributions were carried out at the Jet Propulsory Laboratory, California Institute of Technology, under a contract with the National Aeronautics and Space Administration (80NM0018D0004).

References

Allen, H. M., Crounse, J. D., Bates, K. H., Teng, A. P., Krawiec-Thayer, M. P., Rivera-Rios, J. C., et al. (2018). Kinetics and product yields of the OH initiated oxidation of hydroxymethyl hydroperoxide. *The Journal of Physical Chemistry. A*, *122*(30), 6292–6302. <https://doi.org/10.1021/acs.jpca.8b04577>

Amelynck, C., Schoon, N., & Arijis, E. (2000). Gas phase reactions of CF₃O– and CF₃O–H₂O with nitric, formic, and acetic acid. *International Journal of Mass Spectrometry*, *203*(1-3), 165–175. [https://doi.org/10.1016/S1387-3806\(00\)00321-3](https://doi.org/10.1016/S1387-3806(00)00321-3)

Apel, E. C., Olson, J. R., Crawford, J. H., Hornbrook, R. S., Hills, A. J., Cantrell, C. A., et al. (2012). Impact of the deep convection of isoprene and other reactive trace species on radicals and ozone in the upper troposphere. *Atmospheric Chemistry and Physics*, *12*(2), 1135–1150. <https://doi.org/10.5194/acp-12-1135-2012>

Bahreini, R., Ahmadv, R., McKeen, S. A., Vu, K. T., Dingle, J. H., Apel, E. C., et al. (2018). Sources and characteristics of summertime organic aerosol in the Colorado front range: Perspective from measurements and WRF-Chem modeling. *Atmospheric Chemistry and Physics*, *18*, 8293–8312. <https://doi.org/10.5194/acp-18-8293-2018>

Barth, M. C., Bela, M. M., Fried, A., Wennberg, P. O., Crounse, J. D., Clair, J. M. S., et al. (2016). Convective transport and scavenging of peroxides by thunderstorms observed over the central U.S. during DC3. *Journal of Geophysical Research: Atmospheres*, *121*, 4272–4295. <https://doi.org/10.1002/2015JD024570>

Barth, M. C., Cantrell, C. A., Brune, W. H., Rutledge, S. A., Crawford, J. H., Huntrieser, H., et al. (2015). The deep convective clouds and chemistry (DC3) field campaign. *Bull. Amer. Meteor. Soc.*, *96*(8), 1281–1309. <https://doi.org/10.1175/BAMS-D-13-00290.1>

Barth, M. C., Kim, S.-W., Skamarock, W. C., Stuart, A. L., Pickering, K. E., & Ott, L. E. (2007). Simulations of the redistribution of formaldehyde, formic acid, and peroxides in the 10 July 1996 stratospheric-tropospheric experiment: Radiation, aerosols, and ozone deep convection storm. *Journal of Geophysical Research*, *112*(D13), n/a. <https://doi.org/10.1029/2006JD008046>

Barth, M. C., Kim, S.-W., Wang, C., Pickering, K. E., Ott, L. E., Stenchikov, G., et al. (2007). Cloud-scale model intercomparison of chemical constituent transport in deep convection. *Atmospheric Chemistry and Physics*, *7*(18), 4709–4731. <https://doi.org/10.5194/acp-7-4709-2007>

Bela, M. M., Barth, M. C., Toon, O. B., Fried, A., Homeyer, C. R., Morrison, H., et al. (2016). Wet scavenging of soluble gases in DC3 deep convective storms using WRF-Chem simulations and aircraft observations. *Journal of Geophysical Research: Atmospheres*, *121*, 4233–4257. <https://doi.org/10.1002/2015JD024623>

Bela, M. M., Barth, M. C., Toon, O. B., Fried, A., Ziegler, C., Cummings, K. A., et al. (2018). Effects of scavenging, entrainment, and aqueous chemistry on peroxides and formaldehyde in deep convective outflow over the central and Southeast United States. *Journal of Geophysical Research: Atmospheres*, *123*, 7594–7614. <https://doi.org/10.1029/2018JD028271>

Betts, A. K., Gatti, L. V., Cordova, A. M., Silva Dias, M. A. F., & Fuentes, J. D. (2002). Transport of ozone to the surface by convective downdrafts at night. *Journal of Geophysical Research*, *107*(D20), 8046. <https://doi.org/10.1029/2000JD000158>

Borbon, A., Ruiz, M., Bechara, J., Aumont, B., Chong, M., Huntrieser, H., et al. (2012). Transport and chemistry of formaldehyde by mesoscale convective systems in West Africa during AMMA 2006. *Journal of Geophysical Research*, *117*(D12), n/a. <https://doi.org/10.1029/2011JD017121>

Carlton, A. G., & Baker, K. R. (2011). Photochemical modeling of the Ozark isoprene volcano: MEGAN, BEIS, and their impacts on air quality predictions. *Environmental Science & Technology*, *45*, 4438–4445. <https://doi.org/10.1021/es200050x>

Cazorla, M., Wolfe, G. M., Bailey, S. A., Swanson, A. K., Arkinson, H. L., & Hanisco, T. F. (2015). A new airborne laser-induced fluorescence instrument for in situ detection of formaldehyde throughout the troposphere and lower stratosphere. *Atmospheric Measurement Techniques*, *8*(2), 541–552. <https://doi.org/10.5194/amt-8-541-2015>

Chan, K. R., Dean-Day, J., Bowen, S. W., & Bui, T. P. (1998). Turbulence measurements by the DC-8 meteorological measurement system. *Geophysical Research Letters*, *25*(9), 1355–1358. <https://doi.org/10.1029/97GL03590>

Chatfield, R. B., & Crutzen, P. J. (1984). Sulfur dioxide in remote oceanic air: Cloud transport of reactive precursors. *Journal of Geophysical Research-Atmospheres*, *89*(D5), 7111–7132. <https://doi.org/10.1029/JD089iD05p07111>

Cohan, D. S., Schultz, M. G., Jacob, D. J., Heikes, B. G., & Blake, D. R. (1999). Convective injection and photochemical decay of peroxides in the tropical upper troposphere: Methyl iodide as a tracer of marine convection. *Journal of Geophysical Research-Atmospheres*, *104*(D5), 5717–5724. <https://doi.org/10.1029/98JD01963>

Cooper, O. R., Eckhardt, S., Crawford, J. H., Brown, C. C., Cohen, R. C., Bertram, T. H., et al. (2009). Summertime buildup and decay of lightning NO_x and aged thunderstorm outflow above North America. *Journal of Geophysical Research*, *114*(D1), 114. <https://doi.org/10.1029/2008JD010293>

Crounse, J. D., McKinney, K. A., Kwan, A. J., & Wennberg, P. O. (2006). Measurement of gas-phase hydroperoxides by chemical ionization mass spectrometry. *Analytical Chemistry*, *78*(19), 6726–6732. <https://doi.org/10.1021/ac0604235>

Crum, T. D., & Alberty, R. L. (1993). The WSR-88D and the WSR-88D operational support facility. *Bull. Amer. Meteor. Soc.*, *74*(9), 1669–1687. [https://doi.org/10.1175/1520-0477\(1993\)074<1669:TWATWO>2.0.CO;2](https://doi.org/10.1175/1520-0477(1993)074<1669:TWATWO>2.0.CO;2)

Dickerson, R. R., Huffman, G. J., Luke, W. T., Nunnermacker, L. J., Pickering, K. E., Leslie, A. C. D., et al. (1987). Thunderstorms: An important mechanism in the transport of air pollutants. *Science*, *235*(4787), 460–465. <https://doi.org/10.1126/science.235.4787.460>

DiGangi, E. A., MacGorman, D. R., Ziegler, C. L., Betten, D., Biggerstaff, M., Bowlan, M., & Potvin, C. K. (2016). An overview of the 29 May 2012 Kingfisher supercell during DC3. *Journal of Geophysical Research: Atmospheres*, *121*, 14,316–14,343. <https://doi.org/10.1002/2016JD025690>

Easter, R. C., & Hales, J. M. (1983). Interpretations of the OSCAR data for reactive gas scavenging. In H. R. Pruppacher, R. G. Semonin, & W. G. N. Slinn (Eds.), *Precipitation Scavenging, Dry Deposition, and Resuspension* (pp. 649–662). New York: Elsevier.

Emmons, L. K., Schwantes, R. H., Orlando, J. J., Tyndall, G., Kinnison, D., Lamarque, J.-F., et al. (2020). The chemistry mechanism in the community earth system model version 2 (CESM2). *Journal of Advances in Modeling Earth Systems*, *12*(4), e2019MS001882. <https://doi.org/10.1029/2019MS001882>

Faloona, I., Tan, D., Brune, W. H., Jaeglé, L., Jacob, D. J., & Kondo, et al. (2000). Observations of HO_x and its relationship with NO_x in the upper troposphere during SONEX. *Journal of Geophysical Research*, *105*(D3), 3771–3783. <https://doi.org/10.1029/1999JD900914>

Fast, J. D., Gustafson, W. I., Easter, R. C., Zaveri, R. A., Barnard, J. C., Chapman, E. G., et al. (2006). Evolution of ozone, particulates, and aerosol direct radiative forcing in the vicinity of Houston using a fully coupled meteorology-chemistry-aerosol model. *Journal of Geophysical Research*, *111*, D21305. <https://doi.org/10.1029/2005JD006721>

Finlayson-Pitts, B.J., Pitts, J.N.J. (1986). Atmospheric Chemistry. Fundamentals and experimental techniques.

Fried, A., Barth, M. C., Bela, M., Weibring, P., Richter, D., Walega, J., et al. (2016). Convective transport of formaldehyde to the upper troposphere and lower stratosphere and associated scavenging in thunderstorms over the Central United States during the 2012 DC3 study. *Journal of Geophysical Research: Atmospheres*, *121*, 7430–7460. <https://doi.org/10.1002/2015JD024477>

- Gerken, T., Wei, D., Chase, R. J., Fuentes, J. D., Schumacher, C., Machado, L. A., et al. (2016). Downward transport of ozone rich air and implications for atmospheric chemistry in the Amazon rainforest. *Atmospheric Environment*, *124*, 64–76. <https://doi.org/10.1016/j.atmosenv.2015.11.014>
- Grell, G. A., Peckham, S. E., Schmitz, R., McKeen, S. A., Frost, G., Skamarock, W. C., & Eder, B. (2005). Fully coupled “online” chemistry within the WRF model. *Atmospheric Environment*, *39*(37), 6957–6975. <https://doi.org/10.1016/j.atmosenv.2005.04.027>
- Guenther, A., Karl, T., Harley, P., Wiedinmyer, C., Palmer, P. I., & Geron, C. (2006). Estimates of global terrestrial isoprene emissions using MEGAN (model of emissions of gases and aerosols from nature). *Atmospheric Chemistry and Physics*, *6*(11), 3181–3210. <https://doi.org/10.5194/acp-6-3181-2006>
- Heath, N. K., Fuelberg, H. E., Tanelli, S., Turk, F. J., Lawson, R. P., Woods, S., & Freeman, S. (2017). WRF nested large-eddy simulations of deep convection during SEAC4RS. *Journal of Geophysical Research: Atmospheres*, *122*, 3953–3974. <https://doi.org/10.1002/2016JD025465>
- Homeyer, C. R., and Bowman, K. P. (2017). Algorithm description document for version 3.1 of the three-dimensional gridded NEXRAD WSR-88D radar (GridRad) dataset (tech. Rep.). GridRad.org. <http://gridrad.org/pdf/GridRad-v3.1-Algorithm-Description.pdf>
- Homeyer, C. R., Pan, L. L., Dorsi, S. W., Avallone, L. M., Weinheimer, A. J., & O'Brien (2014). Convective transport of water vapor into the lower stratosphere observed during double-tropopause events. *Journal of Geophysical Research: Atmospheres*, *119*, 10,941–10,958. <https://doi.org/10.1002/2014JD021485>
- Huey, L. G., Villalta, P. W., Dunlea, E. J., Hanson, D. R., & Howard, C. J. (1996). Reactions of CF₃O- with atmospheric trace gases. *The Journal of Physical Chemistry*, *100*(1), 190–194. <https://doi.org/10.1021/jp951928u>
- Jaeglé, L., Jacob, D. J., Brune, W. H., Faloon, I., Tan, D., Heikes, B. G., et al. (2000). Photochemistry of HO_x in the upper troposphere at northern midlatitudes. *Journal of Geophysical Research*, *105*(D3), 3877–3892. <https://doi.org/10.1029/1999JD901016>
- Jaeglé, L., Jacob, D. J., Wennberg, P. O., Spivakovskiy, C. M., Hanisco, T. F., Lanzendorf, E. J., & Hints, et al. (1997). Observed OH and HO₂ in the upper troposphere suggest a major source from convective injection of peroxides. *Geophysical Research Letters*, *24*(24), 3181–3184. <https://doi.org/10.1029/97GL03004>
- Jost, A., Szakáll, M., Diehl, K., Mitra, S. K., & Borrmann, S. (2017). Chemistry of riming: The retention of organic and inorganic atmospheric trace constituents. *Atmospheric Chemistry and Physics*, *17*(16), 9717–9732. <https://doi.org/10.5194/acp-17-9717-2017>
- Kaiser, J., Jacob, D. J., Zhu, L., Travis, K. R., Fisher, J. A., Abad, G., et al. (2018). High-resolution inversion of OMI formaldehyde columns to quantify isoprene emission on ecosystem-relevant scales: Application to the southeast US. *Atmospheric Chemistry and Physics*, *18*(8), 5483–5497. <https://doi.org/10.5194/acp-18-5483-2018>
- Kim, S., Huey, L. G., Stickel, R. E., Tanner, D. J., Crawford, J. H., Olson, J. R., et al. (2007). Measurement of HO₂NO₂ in the free troposphere during the intercontinental chemical transport experiment—North America 2004. *Journal of Geophysical Research-Atmospheres*, *112*(D12), D12S01. <https://doi.org/10.1029/2006JD007676>
- Knote, C., Tuccella, P., Curci, G., Emmons, L., Orlando, J. J., Madronich, S., et al. (2015). Influence of the choice of gas-phase mechanism on predictions of key gaseous pollutants during the AQMEII phase-2 intercomparison. *Atmospheric Environment*, *115*, 553–568. <https://doi.org/10.1016/j.atmosenv.2014.11.066>
- Lawrence, M. G., & Crutzen, P. J. (1998). The impact of cloud particle gravitational settling on soluble trace gas distributions. *Tellus Series B: Chemical and Physical Meteorology*, *50*(3), 263–289. <https://doi.org/10.3402/tellusb.v50i3.16129>, <https://doi.org/10.3402/tellusb.v50i3.16129>
- Lawson, R. P., Stewart, R. E., & Angus, L. J. (1998). Observations and numerical simulations of the origin and development of very large snowflakes. *Journal of the Atmospheric Sciences*, *55*(21), 3209–3229. [https://doi.org/10.1175/1520-0469\(1998\)055<3209:OANSOT>2.0.CO;2](https://doi.org/10.1175/1520-0469(1998)055<3209:OANSOT>2.0.CO;2)
- Leriche, M., Pinty, J. P., Mari, C., & Gazen, D. (2013). A cloud chemistry module for the 3-D cloud-resolving mesoscale model Meso-NH with application to idealized cases. *Geoscientific Model Development*, *6*, 1275–1298. <https://doi.org/10.5194/gmd-6-1275-2013>
- Li, Y., Pickering, K. E., Barth, M. C., Bela, M. M., Cummings, K. A., & Allen, D. J. (2019). Wet scavenging in WRF-Chem simulations of parameterized convection for a severe storm during the DC3 field campaign. *Journal of Geophysical Research*, *124*, 7413, 2019JD030484–7428. <https://doi.org/10.1029/2019JD030484>
- Madronich, S., & Flocke, S. (1997). *Theoretical Estimation of Biologically Effective UV Radiation at the Earth's Surface NATO ASI Series*, (Vol. 52). Berlin: Springer-Verlag.
- Mari, C., Jacob, D. J., & Bechtold, P. (2000). Transport and scavenging of soluble gases in a deep convective cloud. *Journal of Geophysical Research*, *105*(D17), 22255–22267. <https://doi.org/10.1029/2000JD900211>
- McDonald, B. C., McKeen, S. A., Cui, Y. Y., Ahmadov, R., Kim, S.-W., Frost, G. J., et al. (2018). Modeling ozone in the eastern U.S. using a fuel-based mobile source emissions inventory. *Environmental Science & Technology*, *52*(13), 7360–7370. <https://doi.org/10.1021/acs.est.8b00778>
- Neu, J. L., & Prather, M. J. (2012). Toward a more physical representation of precipitation scavenging in global chemistry models: Cloud overlap and ice physics and their impact on tropospheric ozone. *Atmospheric Chemistry and Physics*, *12*, 3289–3310.
- O'Sullivan, D. W., Lee, M., Noone, B. C., & Heikes, B. G. (1996). Henry's law constant determinations for hydrogen peroxide, methyl hydroperoxide, hydroxymethyl hydroperoxide, ethyl hydroperoxide, and peroxyacetic acid. *The Journal of Physical Chemistry*, *100*(8), 3241–3247. <https://doi.org/10.1021/jp951168n>
- Pfister, G. G., Avise, J., Wiedinmyer, C., Edwards, D. P., Emmons, L. K., Diskin, G. D., et al. (2011). CO source contribution analysis for California during ARCTAS-CARB. *Atmospheric Chemistry and Physics*, *11*(15), 7515–7532. <https://doi.org/10.5194/acp-11-7515-2011>
- Pickering, K. E., Thompson, A. M., Scala, J. R., Tao, W.-K., Dickerson, R. R., & Simpson, J. (1992). Free tropospheric ozone production following entrainment of urban plumes into deep convection. *Journal of Geophysical Research-Atmospheres*, *97*(D16), 17985–18,000. <https://doi.org/10.1029/92JD01716>, <https://doi.org/10.1029/92JD01716>
- Pollack, I. B., Lerner, B. M., & Ryerson, T. B. (2010). Evaluation of ultraviolet light-emitting diodes for detection of atmospheric NO₂ by photolysis-chemiluminescence. *Journal of Atmospheric Chemistry*, *65*(2-3), 111–125. <https://doi.org/10.1007/s10874-011-9184-3>
- Richter, D., Weibring, P., Walega, J. G., Fried, A., Spuler, S. M., & Taubman, M. S. (2015). Compact highly sensitive multi-species airborne mid-IR spectrometer. *Applied Physics B: Lasers and Optics*, *119*(1), 119–131. <https://doi.org/10.1007/s00340-015-6038-8>
- Ryerson, T. B., Williams, E. J., & Fehsenfeld, F. C. (2000). An efficient photolysis system for fast-response NO₂ measurements. *Journal of Geophysical Research*, *105*(D21), 26447–26461. <https://doi.org/10.1029/2000JD900389>, <https://doi.org/10.1029/2000JD900389>
- Sachse, G. W., Hill, G. F., Wade, L. O., & Perry, M. G. (1987). Fast-response, high-precision carbon monoxide sensor using a tunable diode laser absorption technique. *Journal of Geophysical Research*, *92*(D2), 2071–2081. <https://doi.org/10.1029/JD092iD02p02071>
- Sadowy, G. A., Berkun, A. C., Chun, W., Im, E., Durden, S. L. (2003). Development of an advanced airborne precipitation radar. (technical feature) [WWW document]. Microwave journal. URL (accessed 3.12.19).

- Sandu, A., & Sander, R. (2006). Technical note: Simulating chemical systems in Fortran90 and Matlab with the kinetic PreProcessor KPP-2.1. *Atmospheric Chemistry and Physics*, 6(1), 187–195. <https://doi.org/10.5194/acp-6-187-2006>
- Snider, J. R., & Huang, J. (1998). Factors influencing the retention of hydrogen peroxide and molecular oxygen in rime ice. *Journal of Geophysical Research*, 103(D1), 1405–1415. <https://doi.org/10.1029/97JD02847>
- Snow, J. A., Heikes, B. G., Shen, H., O'Sullivan, D. W., Fried, A., & Walega, J. (2007). Hydrogen peroxide, methyl hydroperoxide, and formaldehyde over North America and the North Atlantic. *Journal of Geophysical Research*, 112(D12), D12S07. <https://doi.org/10.1029/2006JD007746>
- St. Clair, J. M., McCabe, D. C., Crouse, J. D., Steiner, U., & Wennberg, P. O. (2010). Chemical ionization tandem mass spectrometer for the in situ measurement of methyl hydrogen peroxide. *Review of Scientific Instruments*, 81(9), 094102. <https://doi.org/10.1063/1.3480552>
- Stuart, A. L., & Jacobson, M. Z. (2004). Chemical retention during dry growth riming. *Journal of Geophysical Research*, 109(D7), D07305. <http://doi.org/10.1029/2003JD004197>
- Stuart, A. L., & Jacobson, M. Z. (2006). A numerical model of the partitioning of trace chemical solutes during drop freezing. *Journal of Atmospheric Chemistry*, 53(1), 13–42. <https://doi.org/10.1007/s10874-006-0948-0>
- Tilmes, S., Lamarque, J.-F., Emmons, L. K., Kinnison, D. E., Ma, P.-L., Liu, X., et al. (2015). Description and evaluation of tropospheric chemistry and aerosols in the Community Earth System Model (CESM1.2). *Geoscientific Model Development*, 8(5), 1395–1426. <https://doi.org/10.5194/gmd-8-1395-2015>
- Toon, O. B., Maring, H., Dibb, J., Ferrare, R., Jacob, D. J., Jensen, E. J., et al. (2016). Planning, implementation, and scientific goals of the studies of emissions and atmospheric composition, clouds and climate coupling by regional surveys (SEAC4RS) field mission. *Journal of Geophysical Research: Atmospheres*, 121, 4967–5009. <https://doi.org/10.1002/2015JD024297>
- Travis, K. R., Jacob, D. J., Fisher, J. A., Kim, P. S., Marais, E. A., Zhu, L., et al. (2016). Why do models overestimate surface ozone in the Southeast United States? *Atmospheric Chemistry and Physics*, 16(21), 13561–13577. <https://doi.org/10.5194/acp-16-13561-2016>
- Vay, S. A., Choi, Y., Vadrevu, K. P., Blake, D. R., Tyler, S. C., Wisthaler, A., et al. (2011). Patterns of CO₂ and radiocarbon across high northern latitudes during International Polar Year 2008. *Journal of Geophysical Research*, 116(D14), 116. <https://doi.org/10.1029/2011JD015643>
- Voisin, D., Legrand, M., & Chaumerliac, N. (2000). Scavenging of acidic gases (HCOOH, CH₃COOH, HNO₃, HCl, and SO₂) and ammonia in mixed liquid-solid water clouds at the Puy de Dôme mountain (France). *Journal of Geophysical Research*, 105(D5), 6817–6835. <https://doi.org/10.1029/1999JD900983>
- von Blohn, N., Diehl, K., Mitra, S. K., & Borrmann, S. (2011). Wind tunnel experiments on the retention of trace gases during riming: Nitric acid, hydrochloric acid, and hydrogen peroxide. *Atmospheric Chemistry and Physics*, 11(22), 11569–11579. <https://doi.org/10.5194/acp-11-11569-2011>
- Warneke, C., de Gouw, J. A., Del Negro, L., Brioude, J., McKeen, S., Stark, H., et al. (2010). Biogenic emission measurement and inventories determination of biogenic emissions in the eastern United States and Texas and comparison with biogenic emission inventories. *Journal of Geophysical Research*, 115, 115. <https://doi.org/10.1029/2009JD012445>
- Wiedinmyer, C., Akagi, S. K., Yokelson, R. J., Emmons, L. K., Al-Saadi, J. A., Orlando, J. J., & Soja, A. J. (2011). The fire INventory from NCAR (FINN): A high resolution global model to estimate the emissions from open burning. *Geoscientific Model Development*, 4(3), 625–641. <https://doi.org/10.5194/gmd-4-625-2011>
- Wolfe, G. M., Kaiser, J., Hanisco, T. F., Keutsch, F. N., de Gouw, J. A., Gilman, J. B., et al. (2016). Formaldehyde production from isoprene oxidation across NO_x regimes. *Atmospheric Chemistry and Physics*, 16(4), 2597–2610. <https://doi.org/10.5194/acp-16-2597-2016>
- Yang, Q., Easter, R. C., Campuzano-Jost, P., Jimenez, J. L., Fast, J. D., Ghan, S. J., & Wang, et al. (2015). Aerosol transport and wet scavenging in deep convective clouds: A case study and model evaluation using a multiple passive tracer analysis approach. *Journal of Geophysical Research: Atmospheres*, 120, 8448–8468. <https://doi.org/10.1002/2015JD023647>